Grain size dependence of microscopic strain distribution in a high entropy alloy at the onset of plastic deformation

DOI:
10.1016/j.actamat.2024.120682

Document Version
Accepted author manuscript

Grain size dependence of microscopic strain distribution in a high entropy alloy at the onset of plastic deformation

Biaobiao Yang [a, b], Xu Xu [c, d, *], David Lunt [c, e], Fan Zhang [f, g], Michael D. Atkinson [c, e], Yunping Li [h], Javier Llorca [a, b, *], Xiaorong Zhou [c]

[a] IMDEA Materials Institute, C/Eric Kandel 2, Getafe, 28906 - Madrid, Spain
[b] Department of Materials Science, Polytechnic University of Madrid / Universidad Politécnica de Madrid, E.T.S. de Ingenieros de Caminos, 28040 - Madrid, Spain
[c] Department of Materials, University of Manchester, Oxford Road, United Kingdom of Great Britain and Northern Ireland, Manchester, UK
[d] Department of Chemistry and Chemical Engineering, Nanjing University of Science and Technology, Nanjing, China
[e] UK Atomic Energy Authority, Culham Science Centre, United Kingdom of Great Britain and Northern Ireland, Abingdon OX143DB, UK
[f] School of Materials Science and Engineering, Beijing Institute of Technology, Beijing 100081, PR China
[g] National Key Laboratory of Science and Technology on Materials under Shock and Impact, Beijing 100081, PR China
[h] State Key Lab for Powder Metallurgy, Central South University, Changsha, 410083, China

* Corresponding authors. xu.xu@njust.edu.cn (X. Xu); javier.llorca@upm.es (J. LLorca).

Abstract

The development and distribution of microscopic shear strain have been investigated using high-resolution digital image correlation at the onset of plastic deformation in face-centred cubic CoCrFeNi high entropy alloys with different grain sizes. Microscopic strain localisation increased with grain size as shown by the presence of planar slip traces at the grain level and transgranular bands at the meso-scale. Slip traces were also found within grains larger than a critical size in the fine-grained high entropy alloy, while most of smaller grains were free of slip traces, leading to a bi-modal deformation pattern. Slip traces within coarse grains were associated with the activation of multiple slip systems with lower Schmid factor values, indicating that the local stress state is different from the global one due to the grain-to-grain interactions within the polycrystalline aggregate. In addition, the CoCrFeNi high entropy alloy, -especially the fine-grained one-, exhibits substantially lower microscopic strain heterogeneity as compared to a range of conventional engineering alloys at the onset of plastic deformation.

Keywords: Grain size; Slip trace; Microscopic strain localisation; High entropy alloy; High-resolution digital image correlation (HRDIC).

1. Introduction

High Entropy Alloys (HEAs) have attracted a huge interest during the last two decades due to their particular metallurgy and unique properties [1–4]. HEAs are made up by mixing different metallic elements in a proportion in the range of 5 to 35 at.% for each element. This combination increases the mixing entropy, leading to the formation of a single-phase solid solution with a simple lattice structure, e.g., Face-Centred Cubic (FCC) [5]. The first reported FCC HEA was made up of CoCrFeMnNi (popularly known as the Cantor alloy [6]) and many other alloys based on this system have been developed, including the CoCrNi and CoCrFeNi alloys [7–14].

These FCC HEAs present high strength, ductility and fracture toughness at both ambient and cryogenic temperatures [3] and their deformation mechanisms have been thoroughly investigated [6–14]. Plastic deformation of FCC CoCrFeMnNi alloys is commonly associated with dislocation slip at moderate strain and temperatures (<7.4% true strain at 77 K or <20% true strain at 293 K), whilst deformation twinning arises as an important alternative deformation mode at high strain and/or cryogenic temperatures (>7.4% true strain at 77 K or ~30% true strain near fracture at 293 K) [3,15]. In addition, similar to most FCC metals with a low stacking-fault energy, the dislocation substructure of FCC HEAs evolves from single planar slip on the {111} <110> slip system at low strain (e.g., ~2%) to cross-slip tangled dislocations at moderate strain levels followed by dislocation cell-like structures at high strain (~30%) [16,17]. Stacking faults are observed to be consistent with the dissociation of the dislocations into 1/6<112> Shockley partials [7,17]. However, unlike conventional FCC metals with a high level of slip planarity, dislocation lines in FCC HEAs possess a wavy or tortuous configuration at the nanometre-scale [18,19]. This is attributed to local fluctuations in Peierls barriers [20] or Short-Range Ordering (SRO) [21,22], leading to a lower level of strain localisation in FCC HEAs than in conventional FCC alloys.

The deformation behaviour and mechanical properties of FCC HEAs are dependent on the grain size, crystallographic texture and strain rate [23–25]. For example, the yield strength of the FCC CoCrFeMnNi alloy doubles when the grain size is refined from 155

to 4.4 μm [17]. In particular, the variation of grain size has a significant impact on the deformation mechanisms and the dislocation substructures in FCC HEAs [16,26]. Using Electron Channel Contrast Imaging (ECCI), Liu et al. [27] demonstrated that increasing grain size of NiCoCrFe and $Ni_2CoCrFe$ FCC alloys from ~10 to ~150 μm leads to a transition of dislocation glide from wavy to planar, resulting in a low yield strength but an enhanced strain hardening rate. However, there are very few studies on the effect of grain size on the micromechanisms of plastic deformation in FCC HEAs. In particular, the influence of grain size on microscopic strain distribution within a single grain as well as amongst neighbouring grains in FCC HEAs has been scarcely explored. Most of the experimental investigations on deformation behaviour of FCC HEAs have focussed on Transmission Electron Microscopy (TEM) and ECCI at the nm-scale, and due to the limitations in the region analysed they cannot provide relevant statistical information about the deformation mechanisms at the mesoscale (>> μm) [28–30] or on a grain to grain basis.

In addition, the correlation between grain size and microscopic strain localisation has been reported in conventional engineering alloys [31–35]. For instance, strain localisation in Cu alloys increases as the grain size decreases from ~17 to ~0.4 μm [31]. However, strain localisation during fatigue testing at room temperature in pure Ni decreases of as grain size changes from 290 to 24 μm [34]. These observations highlight the importance of a quantitative analysis with sufficient statistical significance to establish the influence of grain size on the microscopic strain localisation in polycrystalline metals.

A prominent method for resolving deformation at the sub-grain scale across multiple grains is High Resolution Digital Image Correlation (HRDIC). Furthermore, using this technique it is possible to quantify the slip activity in a single slip trace even in grains with multiple active slip systems [36,37]. The combination of high spatial resolution displacement measurement and the fact that single slip traces can be captured allows the identification of the actual active slip systems based on the crystallographic orientation for the grain of interest obtained by orientation mapping. This is achieved by coupling the information provided by slip traces with the adjacent displacement fields using the Relative Displacement Ratio (RDR) method proposed by Chen and Daly [38]. Xu et al.

[39] further validated the active slip systems that were determined using the RDR technique with correlative TEM analysis at the nanometre-scale in a weakly textured Ti-6Al-4V alloy. The determination of the active slip system provides an accurate assessment of deformation mechanisms in a wide range of metallic materials including steels [40–46], Mg- [47–51], Ni- [52–61], Ti- [62–72], and Zr-based alloys [73,74] as well as pure Cu [75,76]. Moreover, the sensitivity of microscopic strain localisation to the grain size was also evaluated using HRDIC in conventional engineering alloys with both homogeneous and bimodal microstructures [33,62,77,78], but it has not been analysed in HEAs.

In this investigation, the influence of grain size on microscopic strain localisation during the early stage of plastic deformation is studied using HRDIC in FCC CoCrFeNi HEA alloys processed following different thermomechanical heat treatments. Intragranular plastic strain is statistically analysed on a grain-to-grain basis to understand the effect of grain size on slip activation and strain heterogeneity. In addition, the active slip modes are determined within grains of typical morphology and size for each condition using a combination of slip trace and RDR analysis coupling with grain orientation information obtained by Electron Back-Scattered Diffraction (EBSD). This analysis has been used to assess the influence of microstructural features, especially grain size, on the mechanisms of microscopic plastic deformation in FCC HEAs. Finally, a quantitative comparison of strain heterogeneity between HEAs and conventional engineering alloy is carried out, and the underlying mechanisms are discussed.

2. Materials and experimental techniques

2.1. Materials

An equiatomic CoCrFeNi ingot was prepared from raw materials with purities > 99.5% in an arc melting furnace with an Ar-filled protective atmosphere, followed by solid-solution treatment at 1200°C for 2 hours. The actual composition of CoCrFeNi alloy was determined using energy dispersive spectroscopy inside the Scanning Electron Microscope (SEM), as presented in **Table 1**. The ingot was sectioned into two pieces and then rolled to a thickness reduction of 90% at room and cryogenic (~-160 ± 10°C)

temperatures, respectively, before annealing at 870°C and 800°C for 1 hour, respectively, followed by final quenching in water. The rolling process was carried out at cryogenic temperature to obtain a more refined grain structure as compared to room temperature due to retarded grain growth. In the following sections, the alloys rolled at the room temperature and annealed at 870°C as well as rolled at the cryogenic temperature and annealed at 800°C, respectively, are referred to as CG (Coarse-Grained) and FG (Fine-Grained) HEAs.

Table 1. Composition of CoCrFeNi alloy in weight and atomic percents.

Element	wt.%	at.%
Co	26.4	25.2
Cr	23.6	25.6
Fe	24.7	24.9
Ni	25.3	24.3

2.2. Mechanical tests

Flat dog-bone tensile specimens were machined with the longitudinal direction parallel to the rolling direction using Electric Discharge Machining (EDM) and immersed in a cooling liquid to avoid any increase in temperature. The specimen dimensions were 15 mm gauge length and 5 mm gauge width with a thickness of 2.5 mm. The macroscopic mechanical properties in tension were measured using an Instron 8501 universal testing machine equipped with an Instron 2620-602 dynamic extensometer at a strain rate of 10^{-3} s^{-1}. Interrupted uniaxial tensile tests of micro tensile specimens, with dimensions of 26 mm gauge length and 3 mm gauge width with a thickness of 1 mm, were carried out at room temperature, using a Kammrath-Weiss 5-kN micro tester at an initial strain rate of 1.6 x 10^{-4} s^{-1} for the HRDIC studies. Deformation was periodically stopped, and the samples were unloaded three times at macroscopic engineering strains of ~0.75%, ~1.50%, and ~2.25% for each condition. For the CG- HEA, the applied plastic strains are ~0.40%, ~1.14%, and ~1.88%, while they are ~0.48%, ~1.22%, and ~1.95% for the FG-HEA. To reduce the effect of the slight differences in plastic strain in the evaluation of the strain heterogeneity, the normalized in-plane effective shear strain relative to the average in-plane effective shear strain was used. Note that macroscopic engineering strain was calculated by dividing the displacement between the grips over the initial gauge length.

Samples were imaged in the Scanning Electron Microscope (SEM) after each loading step to assess the deformation on the surface by means of HRDIC.

2.3. EBSD orientation mapping

The specimens for HRDIC were initially ground to #4000 grit, followed by polishing with diamond suspensions and a final chemo-mechanical polishing in a solution of 1:1.5 amorphous colloidal silica suspension to deionised water ratio to remove the surface deformation introduced during the abrasive stages of preparation. EBSD maps were obtained using a Tescan Mira 3 Field Emission Gun Scanning Electron Microscope (FEG-SEM) equipped with an Oxford Instruments Symmetry CMOS acquisition system at an accelerating voltage of 20 kV and a step size of 0.2 μm. Each map covered an area of 300 × 300 μm with over 2,000,000 datapoints collected from more than 500 grains. The Kikuchi patterns were collected at a resolution of 156 × 128 pixels, a beam current of ~10 nA and an exposure time of ~1 ms with an indexing rate > 95% confidence. The average value and standard deviation of grain size were calculated based on the equivalent diameter of 3,815 and 29,175 grains for the CG and FG-HEAs, respectively.

2.4. High-resolution digital image correlation

After EBSD analysis, the surface was coated with a nano-sized Au speckle pattern following the procedure developed by Gioacchino and da Fonseca [79]. Firstly, the specimen was coated with a ~5 nm thin film of 99.99% Au using an Edwards S150B sputter coater (40 mA for 315 seconds). The continuous film was remodelled by heating at 275°C in a flow of water vapour for 4 hours, leading to the formation of nano-sized Au speckles. For HRDIC analysis, images before and after deformation were obtained in a high-resolution FEI Magellan FEG-SEM in Back-Scattered Electron (BSE) imaging mode, using a Concentric Back-Scattered (CBS) detector. The working distance was 3.5 mm, at an accelerating voltage 5 kV and beam current of 0.8 nA. Mosaics of 19 × 19 images were collected using the microscope's automated mapping software. The mosaics were captured using a 3-point autofocus correlation and with a 20% overlap between tiles to ensure that the whole of the region was focussed and there was sufficient overlap to stitch neighbouring images together. The total areas imaged were 131 × 140 μm and 111 × 118

μm, respectively, for the CG and FG-HEAs. Representative regions of the overall dataset collected were selected within these areas for the detail analysis based on both microstructure and the strain response. Each single image was captured at a resolution of 2,048 × 1,768 pixels and had a horizontal field of view of 30 μm.

The mosaics for the undeformed and deformed states were stitched and aligned using the Fiji's grid/collection function [80,81] and then correlated using the LaVision's DIC software (version DaVis 8.4.0). A standard Fast Fourier Transform cross-correlation relative to the original undeformed image was used to calculate the displacements. The correlation was performed using a sub-window size of 12 x 12 pixels and no overlap, which provides a spatial resolution of ~175 nm. The correlation produces full-field in-plane displacement maps u (x, y, 0) on the x-y plane with normal z, allowing the determination of the in-plane strain tensors. The in-plane effective shear strain, γ_{eff} was calculated according to:

$$\gamma_{\mathrm{eff}} = \sqrt{\left(\frac{\varepsilon_{11}-\varepsilon_{22}}{2}\right)^2 + {\varepsilon_{12}}^2} \quad (1)$$

where $\varepsilon_{11} = \frac{\partial u_x}{\partial x}$ is the axial strain along the loading direction, $\varepsilon_{22} = \frac{\partial u_y}{\partial y}$ the transverse strain along normal in-plane direction, and $\varepsilon_{12} = \left(\frac{\partial u_y}{\partial x} + \frac{\partial u_x}{\partial y}\right)/2$ the in-plane shear strain.

The HRDIC data were analysed using the open-source DefDAP library (Deformation Data Analysis in Python, [82]) and the corresponding graphs were plotted using the Matplotlib module [83]. The active slip system in each individual grain was identified using a combination of slip trace analysis that provides the information of slip plane and the RDR technique that determines slip direction in the slip plane. A typical example of this analysis is shown in **Table 2** and **Appendix Fig. S1**. Parallel slip traces with the same angle in a single grain were treated as one active single slip system, and an acceptance angle of 5° was chosen following the standard convention in slip trace analysis [84]. The grains containing one, two and three families of parallel slip traces were classified as 'single slip', 'double slip' and 'triple slip' grains, respectively.

Table 2. Summary of EBSD-based slip trace analysis and theoretical RDR analysis for each slip system considered for the grain CG-2 highlighted in **Fig. 7 (C)**. Given the experimental slip trace angle is 126.9° and the experimental RDR is -1.910 (cf. **Appendix Fig. S1**), the active slip system in **Fig. 7 (C)** is identified as $(\bar{1}11)$ $[\bar{1}\bar{1}0]$ (Schmid factor = 0.441), as shown in **Table 2** in bold.

Slip plane	Slip direction	Schmid Factor (SF)	SF ranking	Slip trace angle (°)	RDR
(111)	$[01\bar{1}]$	0.242	6th	33.4	-0.784
	$[10\bar{1}]$	0.408	2nd		3.423
	$[1\bar{1}0]$	0.166	8th		0.390
$(11\bar{1})$	[011]	0.033	11th	19.4	0.056
	[101]	0.297	4th		1.154
	$[\bar{1}10]$	0.330	3rd		0.390
$(\bar{1}11)$	$[0\bar{1}1]$	0.272	5th	**125.0**	-0.784
	$[\bar{1}0\bar{1}]$	0.169	7th		1.154
	$[\bar{1}\bar{1}0]$	**0.441**	**1st**		**-2.198**
$(1\bar{1}1)$	$[0\bar{1}\bar{1}]$	0.002	12th	94.9	0.056
	$[\bar{1}01]$	0.058	9th		3.423
	[110]	0.056	10th		-2.198

The distribution of microscopic strain within individual grains was quantitatively analysed by calculating the mean value, the 50th percentile and the 99.5th percentile of in-plane effective shear strain. The maximum value of in-plane effective shear strain was excluded from the analysis to remove any outliers from the data. The level of microscopic strain heterogeneity within each grain was then evaluated based on the ratio between the 99.5th percentile and the mean value of in-plane effective shear strain. This result was further correlated with the grain area and the Schmid Factor (SF) of slip systems on a grain-to-grain basis based on the EBSD data.

3. Results

3.1. Grain structures

EBSD maps were obtained to examine the initial grain structure of the CoCrFeNi HEAs. They are shown in **Fig. 1** and provide detailed characteristics on the grain structure and statistical distribution of grain size as well as crystallographic orientation. The initial grain structure is predominantly composed of polygonal-shaped grains with the grain interiors divided by the Σ3 {111} <$1\bar{1}0$> annealing twin boundaries, as shown in **Figs. 1 (A-D)**. The

relative fraction of annealing twin boundaries for the CG and FG-HEAs are similar, 37% and 32%, respectively. In addition, the grain structure of CG-HEA is substantially coarser than that of FG-HEA, with average grain sizes of 8.8 ± 5.1 µm and 2.8 ± 1.5 µm, respectively, with twins being included. The grain size profile distributions (**Figs. 1 (E)** and **(F)**) further indicate that 25% - 75% percentiles are 5.1 - 11.1 µm and 1.7 - 3.3 µm with medians at 7.5 µm and 2.4 µm for the CG and FG-HEAs, respectively. **Figs. 1 (E)** and **(F)** also include inverse pole figures illustrating the crystallographic orientation distributions from the normal direction. They show a relatively weak texture with maximum intensities between 1.5 and 2.0 in multiples of random distribution (m.r.d) for both HEAs and the Kernel Average Misorientations (KAM) measured of both HEAs were also very low (cf. **Appendix Figs. 2 (A)** and **(B)**), with average values of 0.037° and 0.032°, respectively. The distribution of SF was similar for both HEAs because they have equivalent textures (cf. **Appendix Figs. 2 (C)** and **(D)**).

Thus, EBSD maps show large differences in grain size between both conditions but similar twinning fraction and crystallographic texture as well as residual stress state. This enables a controlled comparison of the deformation mechanism depending on grain size in CoCrFeNi HEA.

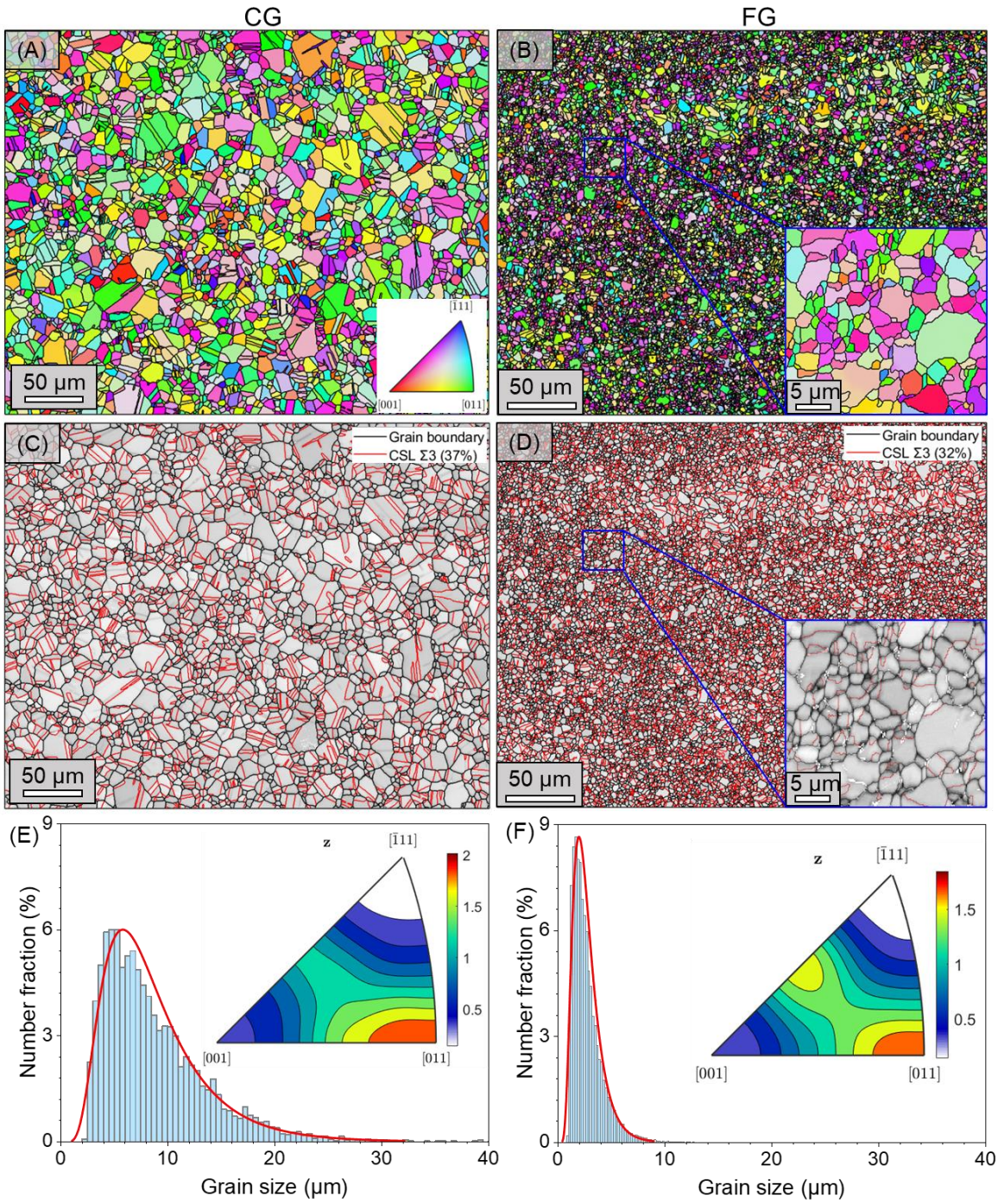

Fig. 1. Grain structure characteristics. The initial grain structures of CoCrFeNi HEAs formed after rolling at (A, C, E) room and (B, D, F) cryogenic temperatures. (A-B) Overlaid images of EBSD Inverse Pole Figure (IPF) - z and grain boundary maps with grain boundaries denoted in black. (C-D) Overlaid images of EBSD band contrast and grain boundary maps with the Coincidence Site Lattice (CSL) Σ3 {111} <1$\bar{1}$0> twinning boundaries denoted in red. (E-F) Grain size distributions. The fitted red curve follows a lognormal distribution. The insets in (E-F) illustrate details of crystallographic distribution as expressed in multiples of random distribution (m.r.d) in the IPFs from the normal direction. The insets in (B, D) show the local magnified images. The loading direction is parallel to the horizontal direction throughout this paper.

3.2. Macroscopic tensile behaviour

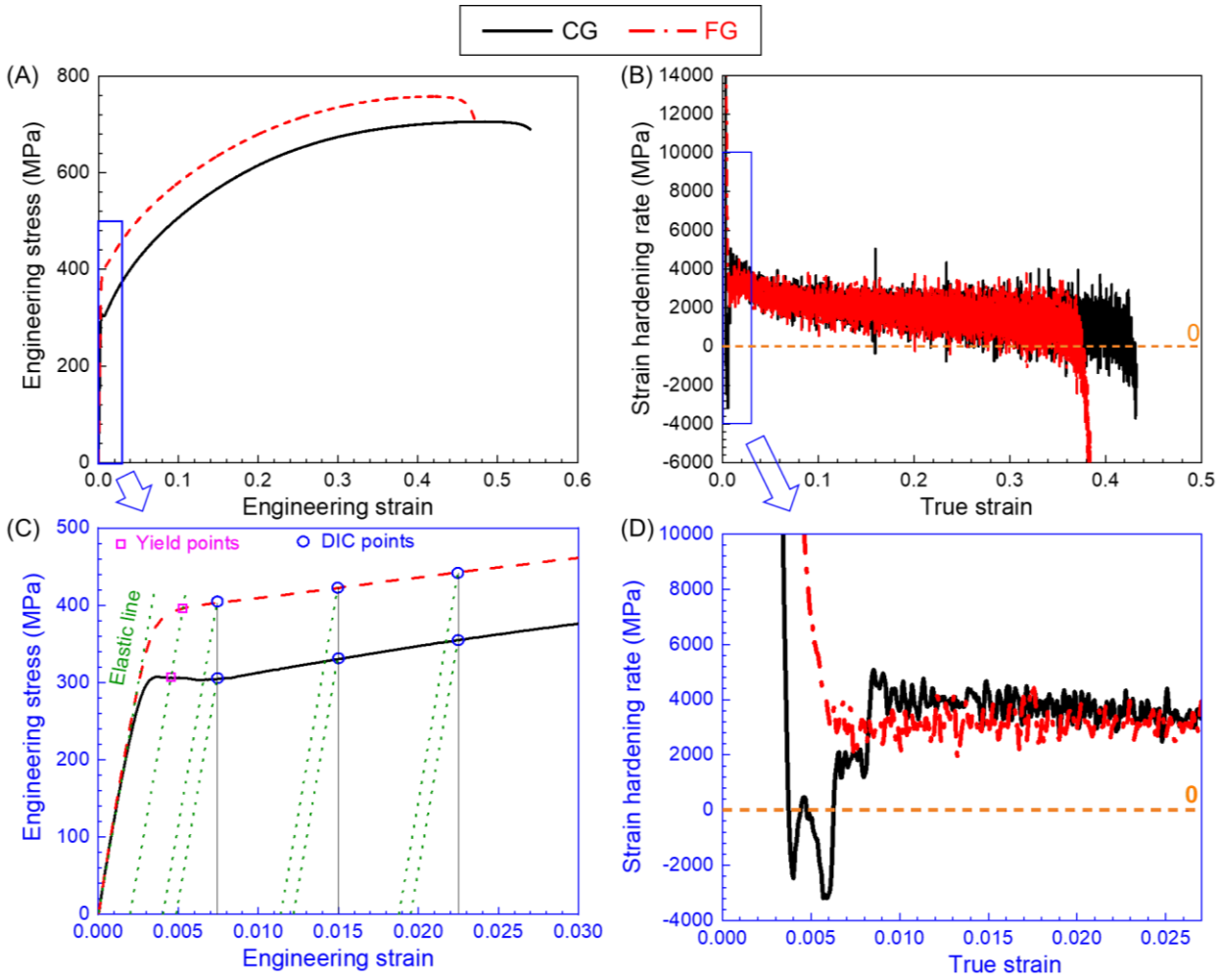

Fig. 2. Tensile behaviour. (A) Engineering stress-engineering strain curves and (B) strain hardening rate-true strain curves for the CG and FG-HEAs. (C, D) Enlarged regions in (A) and (B) revealing the details of the curves at the onset of plastic deformation. The points interrupted for HRDIC analysis are marked by the blue hollow circles in (C).

The engineering stress-engineering strain and strain hardening rate-true strain curves are plotted in **Fig. 2**. The yield strength, ultimate tensile strength, and elongation of both HEAs are indicated in **Table 3**. The yield and ultimate strengths of CG-HEA are 23% and 7% lower than those of the FG-HEA, respectively. The comparison of the strain hardening rates further reveals that the strength improvement of the FG-HEA is mainly achieved during the initial stage of plastic deformation (macroscopic strain < 0.8%) whilst both materials showed similar rates of strain hardening afterwards. Scrutiny of the tensile stress-strain curves reveals a yield plateau at the initial stage of plastic deformation

(between 0.35% and 0.70% strain) in CG-HEA, that is not found in FG-HEA (**Fig. 2 (C)**). It is worth noting that the strain hardening rate of the CG-HEA may become negative in this region (**Fig. 2 (D)**). The stress plateau observed in CG-HEA could be attributed to a longer mean free path for dislocation glide in coarse grains, which inhibits the latent work hardening as dislocations glide on isolated slip planes with limited interaction with other dislocations. The higher hardening rate in FG-HEA at the onset of plastic deformation may be attributed to severe latent hardening within the grains or to the interaction of dislocations with grain / twin boundaries, which reduces the mean free path for dislocation glide [85–87]. However, the actual mechanisms are not clear, and they should be understood to reveal the strengthening induced by grain refinement at the initial stages of plastic deformation in CoCrFeNi HEA.

Table 3. Mechanical properties for CG and FG-HEAs.

Material	Yield strength (MPa)	Ultimate tensile strength (MPa)	Elongation (%)
CG-HEA	306	706	54.1
FG-HEA	396	758	47.1

3.3. Microscopic strain evolution

The microscopic shear strain fields have been analysed in CG and FG-HEAs at the macroscopic strains of ~0.75%, ~1.50%, ~2.25% and they are depicted in **Fig. 3**. Representative enlarged areas showing the differences in microscopic strain localisation between CG and FG-HEAs are provided in **Fig. 4**. The CG-HEA presents intense slip traces in some grains, whilst other grains contain fewer slip traces of low intensity at a macroscopic strain of ~0.75% (**Fig. 3 (A)**). The slip traces exhibit the typical characteristics of planar slip and are finely spaced within individual grain domains defined by grain and annealing twin boundaries (**Appendix Fig. S3**). The presence of intense slip traces is not strongly associated with grain and annealing twin boundaries (**Appendix Fig. S4**). **Figs. 3 (C)** and **(E)** further reveal the development of new slip traces and shear strain intensification at higher macroscopic strains of ~1.50% and ~2.25%. Transgranular strain bands were also observed in CG-HEA, as shown by the continuous slip traces across several neighbouring grains (**Fig. 4 (A)** and **Appendix Fig. S3**).

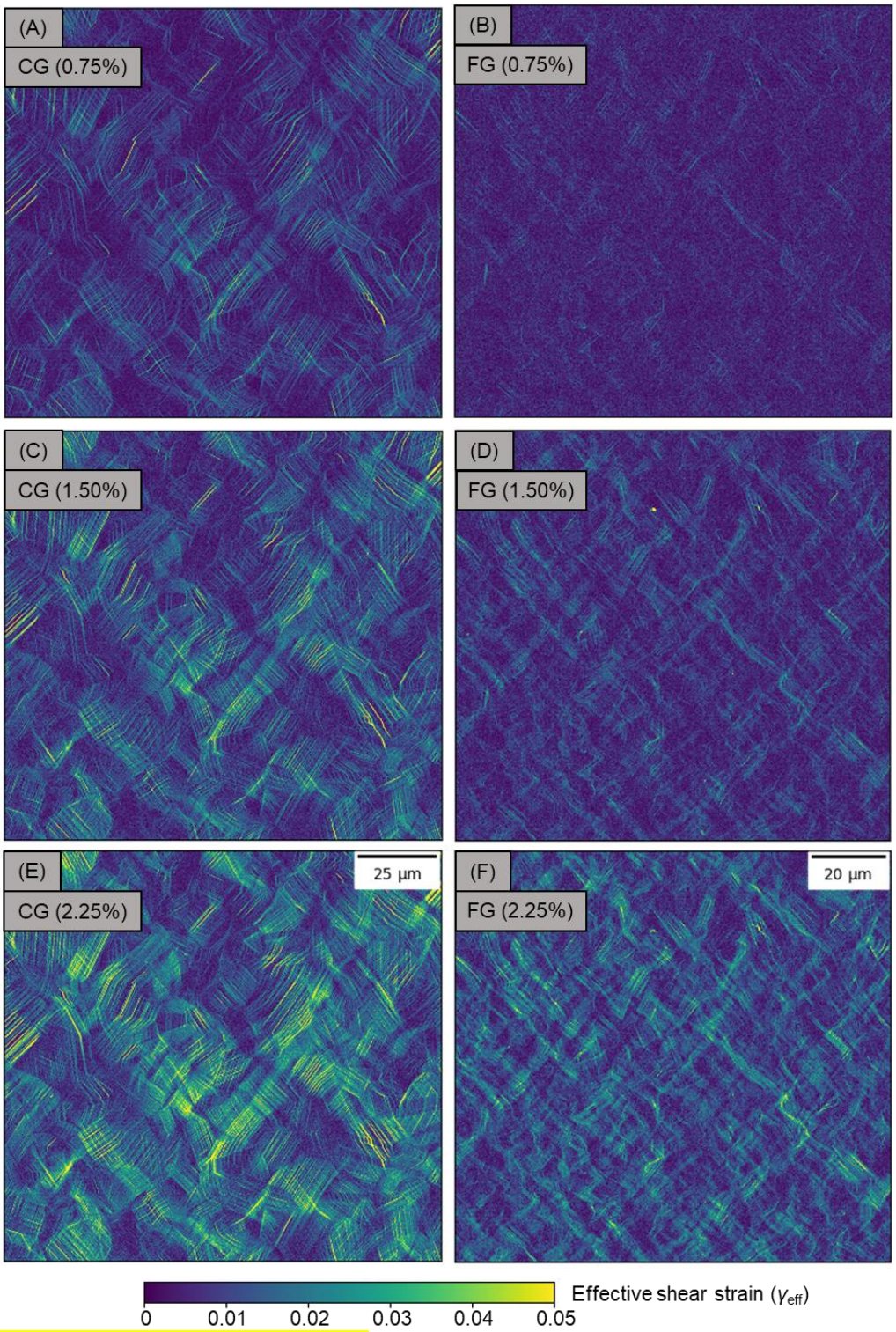

Fig. 3. In-plane effective shear strain maps in (A, C, E) CG and (B, D, F) FG-HEAs at macroscopic strains of (A-B) ~0.75%, (C-D) ~1.50%, (E-F) ~2.25%, respectively. The numbers in top left corner of each map indicate the macroscopic strain applied at each strain step. Overlaid images of in-plane effective shear strain (from HRDIC) and grain / twin boundary (from EBSD) are depicted in **Appendix Fig. S3**.

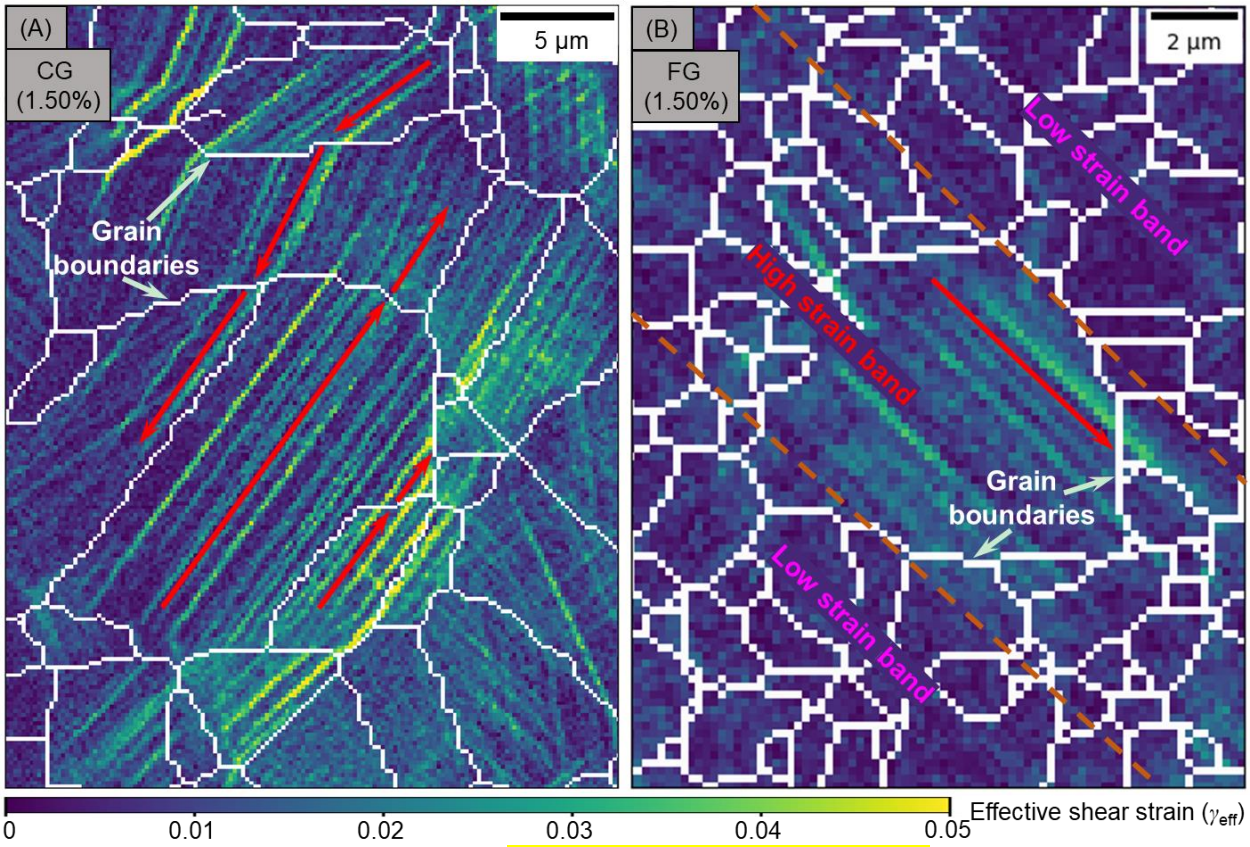

Fig. 4. High resolution maps of the in-plane effective shear strain in (A) CG and (B) FG-HEAs at a macroscopic strain of ~1.50%. Both the grain and Σ3 annealing twin boundaries were overlaid in white on the in-plane effective shear strain maps. The solid arrows in red indicate the traces of the slip planes within individual grains.

In contrast, most grains in FG-HEA contain no slip traces at 0.75% macroscopic strain (**Fig. 3 (B)**) and only a few slightly larger grains show limited slip traces of low intensity. The development of new slip traces and intensification of shear strain were observed in FG-HEA as the applied macroscopic strain increased, as shown in **Figs. 3 (D)** and **(F)**. However, shear strain intensification in the FG-HEA was restricted to large grain agglomerates and their neighbourhood, leading to a bi-modal deformation structure that contains intense slip traces in large 'band-like' regions measuring 3 - 5 µm in width and 10 - 40 µm in length surrounded by regions with very few slip traces (**Fig. 4 (B)**). This result reveals the severe slip trace heterogeneity in the FG-HEA.

The statistical distribution of in-plane effective shear strains within the domain shows that the maximum strain is higher for CG-HEA as compared to FG-HEA in all three strain steps (**Figs. 3** and **5**). The in-plane effective shear strain was normalised by the average in-

plane effective shear strain across the entire map to compensate for the differences in microscopic strain between CG and FG-HEAs (**Fig. 5**).

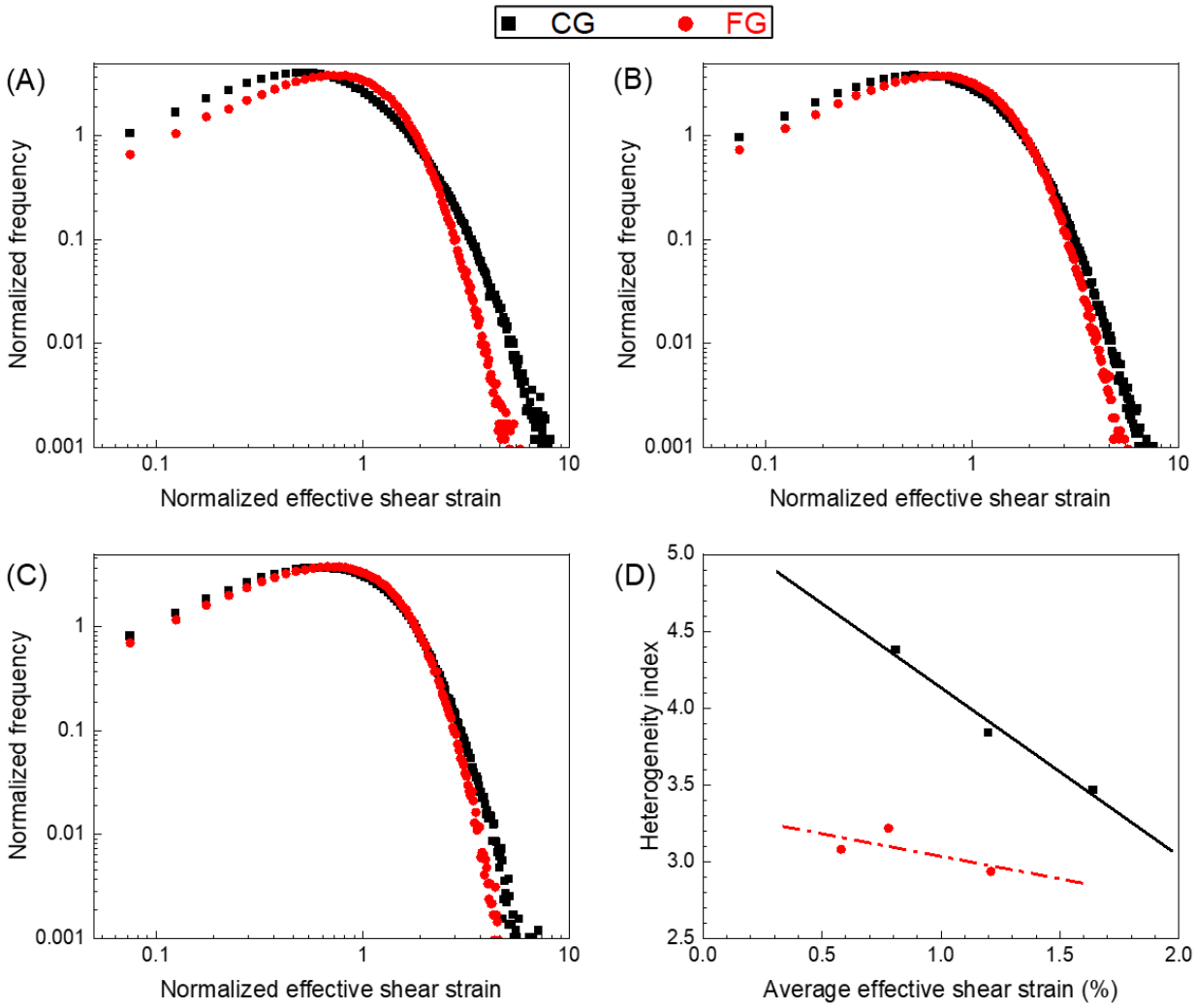

Fig. 5. Quantification of the strain distribution heterogeneity. (A-C) The frequency distribution of in-plane effective shear strain normalised by average in-plane effective shear strain in both CG and FG-HEAs at macroscopic strains of (A) ~0.75%, (B) ~1.50%, and (C) ~2.25%. (D) Evolution of heterogeneity index, i.e., 99.5th percentile of normalised in-plane effective shear strain with respect to the average in-plane effective shear strain.

The frequency distribution of in-plane effective shear strain between CG and FG-HEAs at a macroscopic strain of ~0.75% is plotted in **Fig. 5 (A)**. Notably, the ratio between the maximum in-plane effective shear strain and the average one in the CG-HEA is almost twice than that in the FG-HEA, and this result indicated that the microscopic strain heterogeneity in CG-HEA is higher than that in FG-HEA. This ratio (or microscopic strain heterogeneity) decreases in the CG-HEA as the macroscopic strain increases to ~1.50%

and ~2.25%, as shown in **Figs. 5 (B)** and **(C)**, respectively, but it does not vary strongly with the macroscopic strain in the FG-HEA. It should be noted that the microscopic strain heterogeneity is always higher in the CG-HEA at all strains. The strain heterogeneity index is calculated based on the 99.5th percentile of maximum in-plane effective shear strain to the average in-plane effective shear strain ratio and it is plotted as a function of the applied strain for the CG and the FG-HEAs in **Fig. 5 (D)**. The larger strain heterogeneity index clearly indicates a higher level of microscopic strain localisation in the CG-HEA as compared to the FG-HEA, while the difference in microscopic strain heterogeneity with grain size gradually diminishes at the macroscopic strain increases.

3.4. Grain size dependence of intragranular strain heterogeneity

The distribution of in-plane effective shear strain was further quantified on a grain-to-grain basis to compare the extent of microscopic strain localisation as a function of grain size. **Fig. 6** shows statistical distributions of the 99.5th percentile and average of in-plane effective shear strain as a function of grain size in CG and FG-HEAs and the applied macroscopic strain.

The ratios between the 99.5th percentile and the mean value are in the range of 0.1 - 0.3 for most grains in the CG-HEA at a macroscopic strain of ~0.75% (**Fig. 6 (A)**). The difference between the 99.5th percentile and the mean strain is most pronounced in the largest grains (200 - 500 μm^2) with ratios close to 0.1, although there is not a clear correlation between mean strain values and grain size. The smaller grains are preferentially found close to the boundary defined by the line with a slope of 0.5. This comparison indicates a higher degree of microscopic strain localisation / heterogeneity in coarser grains at the onset of plastic deformation in the CG-HEA. Similar features are found in the CG-HEA at larger macroscopic strains, as shown in **Figs. 6 (C)** and **(E)**. The distribution is gradually rotating in the counterclockwise direction as the macroscopic strain increases. Accordingly, the degree of microscopic strain localisation / heterogeneity of the CG-HEA is less severe with increasing macroscopic strain, in line with the results in **Fig. 5**.

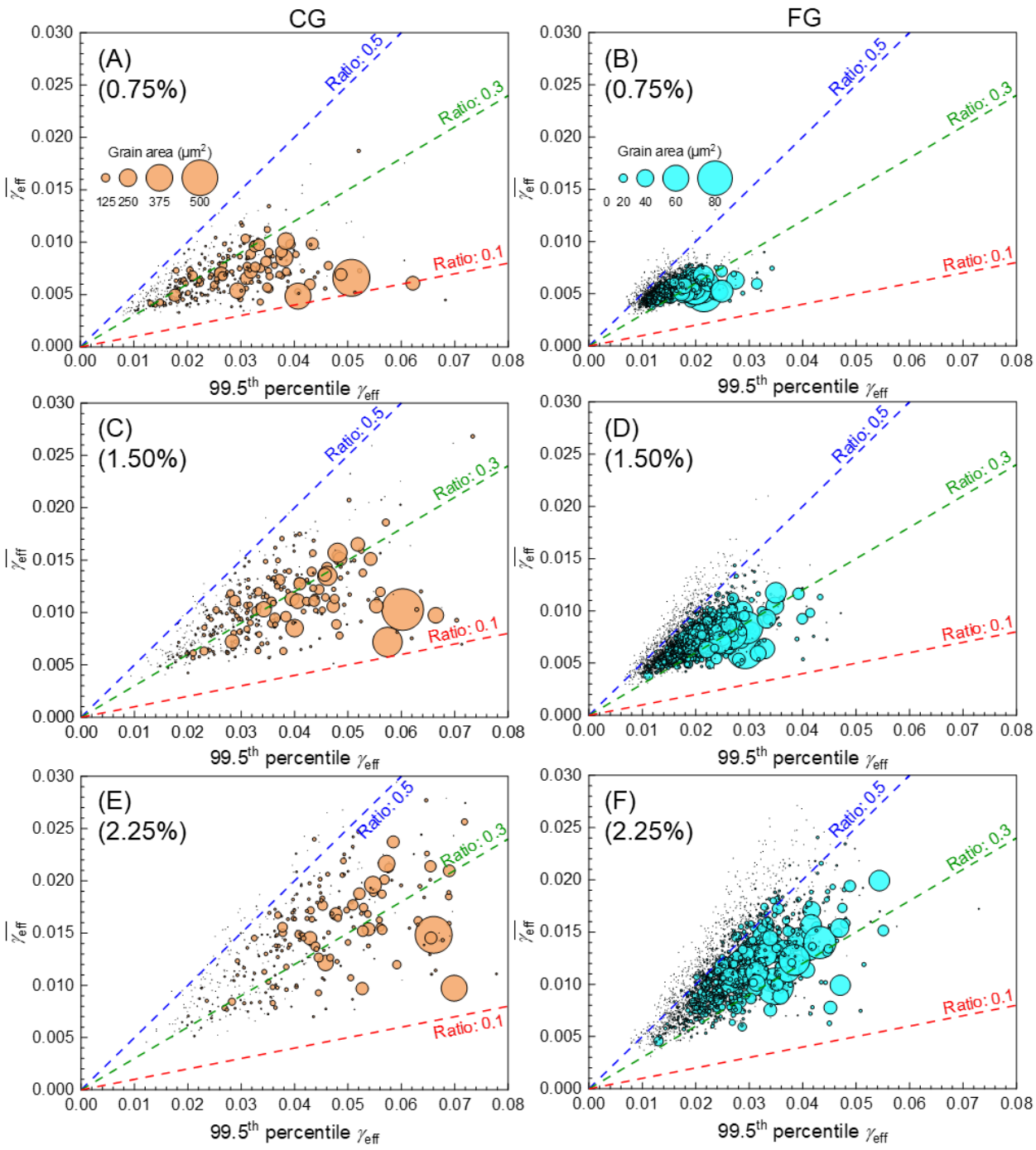

Fig. 6. Microscopic strain heterogeneity as a function of grain size and the applied macroscopic strain. Statistical distribution for the correlation between the 99.5th percentile and the mean value of the in-plane effective shear strain, $\overline{\gamma_{\mathrm{eff}}}$, within individual grain as a function of grain area in (A, C, E) CG and (B, D, F) FG-HEAs at macroscopic strains of (A, B) ~0.75%, (C, D) ~1.50% and (E, F) ~2.25%, respectively. The size of each circle corresponds to the grain area of the individual grain. The numbers on the top left corner indicate the macroscopic applied strain. 579 and 2,873 grains were included in the analysis for CG and FG-HEAs, respectively.

The microscopic strain heterogeneity in FG-HEA is shown in **Figs. 6 (B)**, **(D)**, and **(F)** as a function of the applied macroscopic strain. They also show a higher degree of microscopic strain localisation / heterogeneity in the larger grains, which in good agreement with the results in the CG-HEA. Thus, larger grains show a higher degree of microscopic strain localisation / heterogeneity in CoCrFeNi HEA. Moreover, the degree of microscopic strain heterogeneity decreases with the applied macroscopic strain, as evidenced by the gradually rotated distribution in the counterclockwise direction as the macroscopic strain increases in **Figs. 6 (D)** and **(F)**. This suggests that the microscopic strain localisation / heterogeneity in the FG-HEA also decreases with the macroscopic strain. In addition, the larger grains (i.e., in the range 20 - 80 μm^2) in **Fig. 6 (B)** show lower microscopic strain heterogeneity than the grains in the CG-HEA at similar applied macroscopic strain. The lower boundaries of ratio between the 99.5^{th} percentile and the mean value of the in-plane effective shear strain at macroscopic strains of ~1.50% and ~2.25% are higher in the FG-HEA as compared with the CG-HEA. This is presumably due to the difference between the upper and lower limits of grain sizes for both HEAs.

3.5. Slip behaviour dependence on grain size

To understand the influence of grain size on the distribution of microscopic slip behaviour within the grains, slip traces were examined within the grains of different sizes at a macroscopic strain of ~1.50%. Strain maps for individual grains with examples of the different types of slip, i.e., no slip, single slip, double slip, and triple slip for CG and FG-HEAs at a macroscopic strain of ~1.50% are shown in **Fig. 7**. These examples were chosen to be representative of the overall behaviour that has been quantified in subsequent **Figs. 8** and **9**. To be specific, based on the grain area, slip trace numbers and SF, some representative grains were selected to highlight the grain size dependence on slip behaviour, i.e., the slip trace heterogeneity.

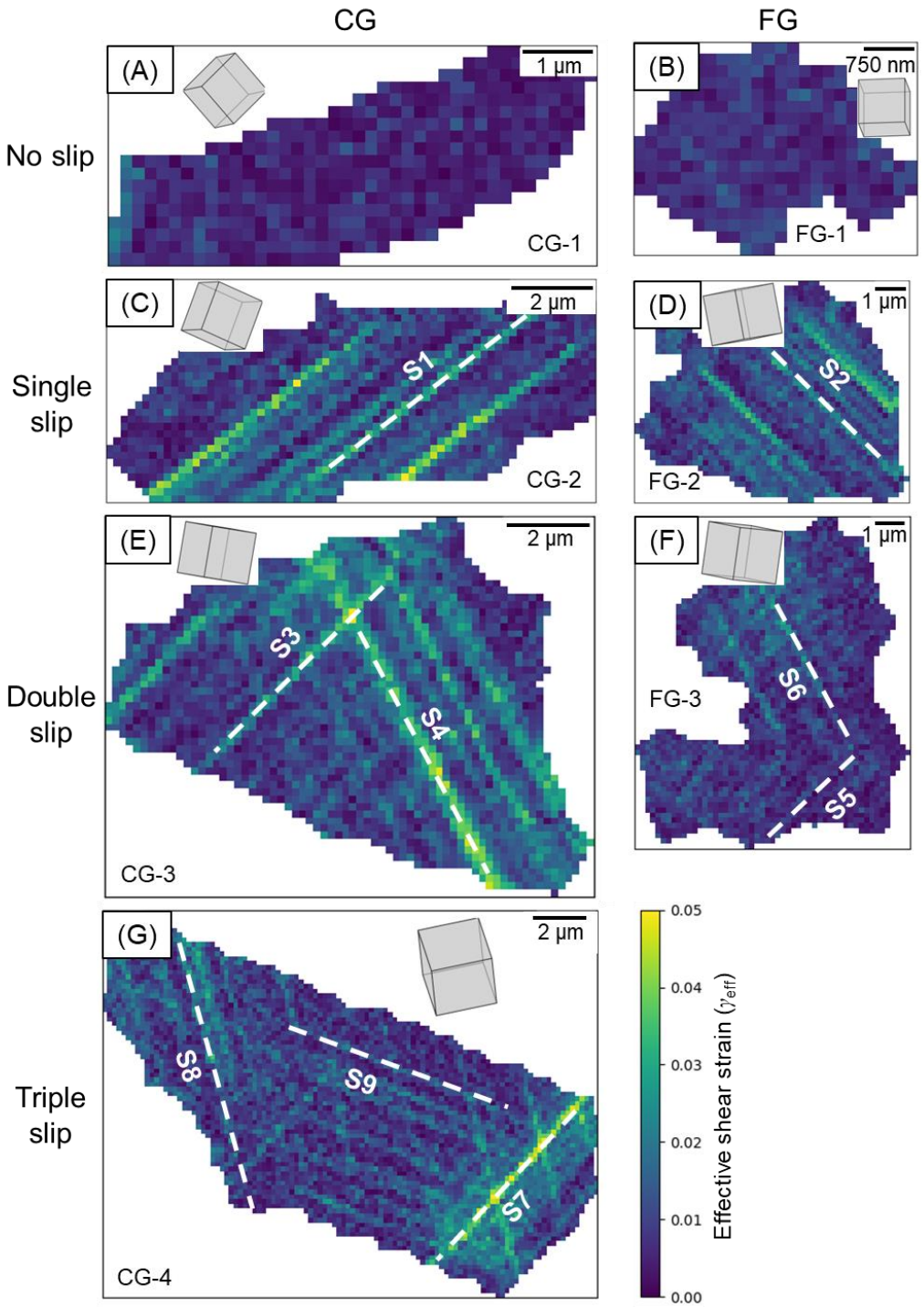

Fig. 7. Slip behaviour within individual grains. HRDIC strain maps showing the distribution of in-plane effective shear strain in the representative grains (A, B) without slip traces and with slip traces on (C, D) one, (E, F) two and (G) three slip systems. (A, C, E, G) correspond to CG-HEA and (B, D, F) to FG-HEA at a macroscopic strain of ~1.50%. The dash lines in white indicate the orientations of slip traces within each grain. Active slip systems were identified using the RDR technique, with the corresponding values of SF calculated based on the grain orientation and the uniaxial macroscopic stress.

Figs. 7 (A) and **(B)** reveal that no visible slip traces were detected for the representative grains with an area < ~20 μm^2 for both CG and FG-HEAs. These grains demonstrate a homogeneous strain distribution with a maximum shear strain of ~0.02. **Figs. 7 (C)** and **(D)** show that the grains containing slip traces associated with one single slip system are finely spaced with a high intensity and a maximum shear strain of ~0.04 in both CG and FG-HEAs. Slip trace analysis in combination with RDR technique further confirmed that all the slip traces were associated with one of the {111} <110> slip systems. Moreover, the SFs for the corresponding slip systems in grains CG-2 and FG-2 were ~0.45, the highest one for the twelve possible {111} <110> slip systems (**Table 4**). **Figs. 7 (E-G)** show the presence of slip traces on multiple slip systems within the larger grains in both CG and FG-HEAs. Slip trace analysis further identified the {111} <110> slip systems for all the detected slip traces. The slip traces within the grains containing two activate slip systems (i.e., the 'double slip' cases) in CG-HEA are typically slip systems with the 2nd or the 3rd largest SF (between 0.33 - 0.42), whilst the SFs corresponding to slip traces in FG-HEA are the 1st or the 2nd largest amongst the twelve {111} <110> slip systems with values > 0.40 (cf. **Table 4**). In addition, the slip traces within a representative grain containing three active slip systems (i.e., the 'triple slip' case) in CG-HEA are distributed on slip systems with lower rankings of SF at 4th, 5th, and 8th with values < 0.40.

Table 4. Summary of features of grains and slips in **Fig. 7**. Note that all the slip systems for the identified grains in **Fig. 7** are tabulated in **Appendix Table S1**.

Grain	Grain area (μm^2)	Slip system		SF	Rank
CG-1	13.5	No slip			
CG-2	45.3	S1	$(\bar{1}11)$ $[\bar{1}\bar{1}0]$	0.441	1st
CG-3	174.7	S3	$(11\bar{1})$ [101]	0.331	3rd
		S4	$(1\bar{1}1)$ [110]	0.420	2nd
CG-4	142.1	S7	$(11\bar{1})$ [011]	0.391	4th
		S8	$(1\bar{1}1)$ $[0\bar{1}\bar{1}]$	0.343	5th
		S9	$(\bar{1}11)$ $[\bar{1}\bar{1}0]$	0.291	8th
FG-1	8.7	No slip			
FG-2	49.2	S2	$(11\bar{1})$ $[\bar{1}\bar{1}0]$	0.461	1st
FG-3	66.1	S5	$(11\bar{1})$ $[\bar{1}\bar{1}0]$	0.477	1st
		S6	$(1\bar{1}1)$ [110]	0.412	2nd

Note that there is a greater uncertainty in the identification of grains with single, double, and triple slip in the FG-HEA because the microscopic strain localisation takes place at the resolution limit of the HRDIC measurements, especially in small grains with multiple slip. In addition, there are 3 different <110> slip directions on a given {111} plane in the FCC lattice but they lead to the same slip trace [59]. Although RDR is able to identify most of them, the identification of multiple active slip systems on the same slip trace is still challenging. The number of active slip systems for grains with various grain areas is plotted in **Fig. 8**, and corresponding statistical distribution for grains having various slipping features is displayed in **Table 5**.

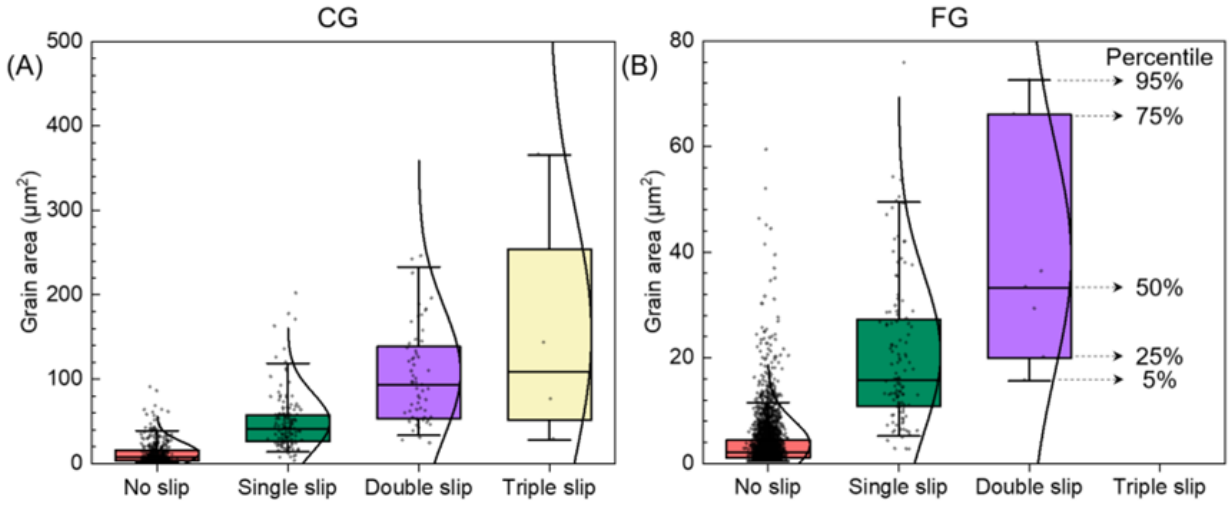

Fig. 8. Statistical distribution for the number of active slip system as a function of grain size. Number of active slip systems as a function of the grain area in (A) CG and (B) FG-HEAs at a macroscopic strain of ~1.50%. The grains without slip traces and those containing slip traces corresponding to one, two and three different slip systems are denoted as 'no slip', 'single slip', 'double slip' and 'triple slip', respectively. Note that the limited numbers of 'Triple slip' in CG and 'Double slip' in FG lead to large standard deviations.

Table 5. Number and number fraction of grains containing different numbers of active slip systems in CG and FG-HEAs at a macroscopic strain of ~1.50%. The total number of grains that were analysed in CG and FG-HEAs are 579 and 2,873, respectively.

Material	Number of grains with slip traces	Single slip	Double slip	Triple slip	Total number of active slip systems
CG-HEA	194	131 (68%)	59 (30%)	4 (2%)	261
FG-HEA	124	117 (94%)	7 (6%)	0	131

The results in **Fig. 8 (A)** demonstrate that no slip traces were found in most of the grains with an area < ~20 μm^2, whilst grains exhibiting slip traces are larger and multiple slip is only found in the largest grains (55 - 200 μm^2 in area) for the CG-HEA. **Table 5** further reveals that amongst the 34% of the grains showing slip traces in CG-HEA, the number of grains containing intragranular slip traces on one single slip system is more than twice the number of grains with more than two slip systems. **Fig. 8 (B)** shows that the grains without slip traces are < ~7.5 μm^2 in area for the FG-HEA, whilst the areas of the grains containing more than two slip systems are in the range of 25 - 60 μm^2. **Table 5** further indicates that the relative fraction of grains containing intragranular slip traces is substantially lower with a measured value of 4% in FG-HEA as compared to CG-HEA in which 34% of the grains exhibit slip traces. Considering the macroscopic plastic strain levels for CG and FG-HEA are comparable (**Fig. 2**), it is very likely that most of the plastic deformation of FG-HEA is absorbed by the deformed grains without clear slip traces.

The active slip systems were further analysed on a grain-to-grain basis and the corresponding SFs were calculated based on the crystallographic orientation of grains and the RDR technique for both CG and FG-HEAs at a macroscopic strain of ~1.50%. **Fig. 9** shows the statistical distribution of the SF for the active slip systems and the number fraction of active slip systems ranked as a function of the 12 theoretical SFs. The SFs of major active slip systems are in the range of 0.25 - 0.50, with a mean value of 0.34 for CG-HEA (**Fig. 9 (A)**). The SFs of major active slip systems are > 0.36, with a mean value of 0.37 for FG-HEA (**Fig. 9 (B)**). The results in **Figs. 9 (C)** and **(D)** indicate that the active slip systems in CG-HEA are the ones with up to the 4th highest SF, whilst the slip systems with up to the 2nd highest SF are predominantly activated in FG-HEA.

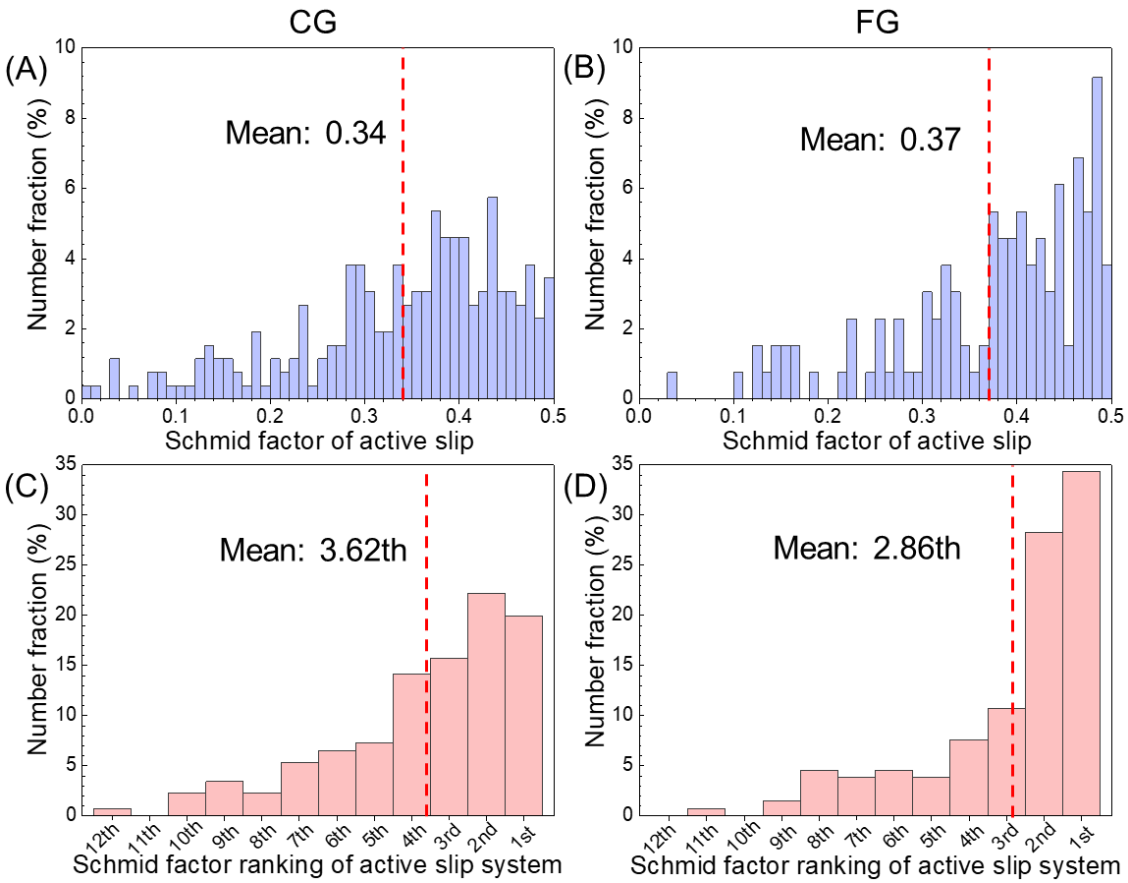

Fig. 9. Distribution of SF for active slip systems. (A, B) Statistical distribution of SFs and (C, D) number fraction of active slip systems ranked as a function of the corresponding SF in (A, C) CG and (B, D) FG-HEAs.

4. Discussion

It is well established that deformation behaviour in most metallic systems is heterogeneous due to slip band formation. HRDIC enables quantitative characterisation of microscopic strain localisation and provides an opportunity to directly compare this microscopic strain localisation during plastic deformation between different alloys and within the same alloy but with different microstructures [67,74]. In the present work, this methodology has been applied to two HEAs with the same composition but different grain sizes to investigate the effect of grain size on the deformation mechanisms. According to previous works on FCC CoCrFeNi HEAs [7,16] and the low strain level during deformation, it is very likely that both Coarse-Grained (CG) and Fine-Grained (FG) HEAs are deformed by planar slip along the {111} <110> slip system.

4.1. Microscopic strain localisation behaviour of HEAs

In CG-HEA, 34% of the grains exhibit distinct slip traces at a macroscopic strain of ~1.50%. These slip traces were classified into 3 main categories, which were 'single slip' (68%), 'double slip' (30%), and 'triple slip' (2%). Statistical analysis further revealed that larger grains activated multiple slip systems (**Fig. 8**), whereas this was not observed in smaller grains. HEAs with coarse grains (~5 μm, corresponding to ~20 μm^2 in area) also showed the trend to activate multiple slip systems, as reported in a FCC CoCrFeMnNi HEA with a heterogeneous grain structure (140 nm to 5 μm) [88]. It should be noted that the coarse grains possess a larger area of grain boundary and grain volume, but the alloy also presents a reduced area fraction of grain boundary and of triple junctions per unit volume [89]. The former indicates that the activation of multiple slip systems within a grain is easier. Assuming that dislocations are preferentially nucleated at or close to grain boundaries [90,91], a larger grain boundary area for one grain implies a higher probability to find a more complex local stress condition that facilitates the activation of anomalous slip systems that are not the most favourable under the macroscopic stress state [92–94]. This hypothesis is supported by the activation of multiple slip systems with low SFs in CG-HEA (**Fig. 7 (G)**), whilst the active slip systems in smaller grains are associated with the 1st and 2nd highest SFs (**Table 4**). The latter, i.e. lower grain boundary area per unit volume, implies a larger mean free path for dislocation glide within an individual grain [85–87]. The activated slip systems can thus accommodate a considerable amount of intragranular strain before the local stress condition is significantly changed due to dislocation pile-up at the grain boundaries. Therefore, slip systems in the 'single / double slip' grains were activated from the early stage of plastic deformation (i.e., ~0.75% macroscopic strain), with no additional slip systems activated during the subsequent deformation stages (**Fig. 3**).

In FG-HEA, distinct slip traces were observed within 4% of the total number of grains at a macroscopic strain of ~1.50%. Given that distinct slip traces are associated with a high level of microscopic strain localisation, the reduced number of grains having slip traces contributes to a lower level of microscopic strain localisation in the FG-HEA as compared to the CG-HEA. In addition, the grains with homogeneous distribution of microscopic

strain are smaller as compared to the grains with distinct slip traces. The grains measuring > 7.5 μm^2 in area typically exhibit slip traces at macroscopic strain of ~1.50%, whilst the grains below the critical size exhibit a relatively homogeneous distribution of microscopic strain without distinguishable slip traces (**Fig. 8**). This is consistent with previous observations that indicate that slip planarity is reduced within the grains < 10 μm during the onset of plastic deformation in the FCC NiCoCrFe and Ni_2CoCrFe alloys [27]. In addition, active slip systems in FG-HEA are predominantly associated with the 1st and 2nd highest SFs, whilst the rank of the SFs of the active slip systems in CG-HEA varies from the 7th to the 1st (**Fig. 9**). This suggests that the microscopic stress state in CG-HEA is more likely to deviate from the global stress as compared to FG-HEA.

Furthermore, the high level of microscopic strain heterogeneity of CG-HEA is attributable to the presence of transgranular strain bands formed the spontaneous localisation of strain in bands encompassing several adjoining grains, as shown in **Fig. 4 (A)** [63,95]. Transgranular strain bands are reported in the majority of metallic systems that have been studied using the HRDIC technique [63,68]. The FG-HEA exhibits a lower degree of transgranular strain band formation as compared to CG-HEA. This is consistent with previous observations that indicate that a reduction in grain size led to a lower number of shear bands in Cu [76].

4.2. Strain heterogeneity comparison between HEA and other engineering alloys

Microscopic strain heterogeneity depends on both the grain size and macroscopic strain for the FCC CoCrFeNi HEA being investigated in this study. The level of strain heterogeneity in HEAs is further compared with a range of conventional engineering alloys at a similar level of strain, as detailed in **Table 6** and **Fig. 10**. The alloys containing precipitates [58,74] and ordered phases [53,54,67] exhibited higher levels of strain heterogeneity as compared to the single-phase solid solution [53]. The presence of incoherent or interphase boundaries promotes microscopic strain localisation via the formation of dislocation pile-ups and co-planar dislocation dipoles. In addition, the presence of strong crystallographic texture leads to intense microscopic strain heterogeneity in the Ti-6Al-4V alloy [63] upon macroscopic loading conditions that favour

slip activation within macrozones. In the present study, the FCC CoCrFeNi HEA has a matrix of single-phase solid solution without significant crystallographic texture, contributing to a relatively low level of microscopic strain localisation / heterogeneity.

In addition, the heterogeneity indexes from FCC Ni-based superalloys, including the Inconel 690 [53] and Inconel 625 [58] alloys, are relatively lower as compared to the Ti-6Al-4V [62,67,68] and Zircaloy-4 [74] alloys that possess an Hexagonal Close-Packed (HCP) lattice structure at a similar macroscopic strain (**Table 6**). This is attributable to a higher number of slip systems that can be activated to accommodate strain within an FCC lattice as compared to an HCP lattice. In the present study, the CoCrFeNi HEA with an FCC lattice structure further exhibits a lower level of strain heterogeneity than the FCC Ni-based alloys containing a single-phase solid solution at a similar strain level. For instance, the heterogeneity indexes of the HEAs with average grain diameters of 8.8 and 2.8 μm are ~59% and ~76% lower than those of Inconel 690 [53] with an average grain diameter of ~9.0 μm. These results highlights a substantially lower level of microscopic strain heterogeneity in the CoCrFeNi HEA than the Ni-based superalloys with similar microstructural characteristics, while a reduction of grain size further decreases microscopic strain heterogeneity, which is generally beneficial for superior ductility (>35% here) and damage tolerance [36,66,96–99].

Based on HRDIC analysis on a wide range of alloys, the amplitude of slip localisation that develops at 0.2% applied macroscopic plastic strain displays a linear dependence on yield strength [36]. However, the reduction of grain size from 41 to 13 μm in René 88 alloy brings a lower microscopic strain localisation amplitude (average normalized max. intensity: ~1.0 to ~0.8 $nm \cdot \mu m^{-1}$) but a higher yield strength (850 to 1025 MPa) [36], in good agreement with this work. In addition, microscopic strain localisation is generally associated with reduced ductility [31,100,101] and fatigue life [66]. For instance, grain refinement of pure Cu leads to the reduction of ductility with a higher level of microscopic strain localisation [31]. However, the reduction of grain size in the Mg-Zn-Zr-Ca alloy improved the ductility with a higher level of strain localisation [32]. Therefore, the relationship among the grain size, strain localisation amplitude, and elongation is still controversial, requiring a further investigation.

Table 6. Microscopic strain heterogeneity and microstructural characteristics of the CoCrFeNi HEAs and other engineering alloys based on the results of HRDIC analysis.

Material	Microstructural characteristics	Grain size (μm)	Macroscopic strain (%)	Heterogeneity index of microscopic strain *
CG-HEA	Single γ phase	8.8 ± 5.1	0.75	8.7
			1.50	5.8
			2.25	4.1
FG-HEA	Single γ phase	2.8 ± 1.5	0.75	4.2
			1.50	2.9
			2.25	2.4
RR1000 [53,54]	γ + γ′ (30% volume fraction + ~70 nm diameter) phases	~15.0	2.00	~25.0
	γ + γ′ (40% volume fraction + ~250 nm diameter) phases	~16.0	2.00	~27.5
Inconel 690 [53]	Single γ phase	~9.0	2.00	~10.0
Inconel 625 [58]	γ phase + carbides on grain boundaries	~7.0	3.00	3.2
Ti-6Al-4V [62,67,68]	α + β phases	~10.0	1.00	11.0-12.0
			5.00	11.0-12.0
	α + β + α_2 (Ti_3Al) phases	~10.0	1.00	21.0-22.0
			5.00	20.0
	α phase without macrozone	~8.0	3.00	8.0
	α phase with macrozone	~8.0	3.00	11.0
Zircaloy-4 [74]	Single α-Zr phase	~10.0	3.00	~4.4
	α-Zr + δ-ZrH + $Zr(Fe,Cr)_2$ phase	~10.0	3.00	~6.8

* Heterogeneity index of microscopic strain is calculated based on the ratio of 99.5th percentile of in-plane effective shear strain to the applied macroscopic strain.

Intrinsically, the relatively homogeneous distribution of microscopic plastic strain in the HEA is attributable to the wavy or tortuous dislocation lines at the nanometre-scale in the FCC HEAs [18,19]. This is fundamentally related with local fluctuations of Peierls barriers [20] or SRO [21,22] in HEAs. Using large-scale molecular dynamic simulations on the FCC CoCrFeMnNi alloy, Wang et al. [22] demonstrated that local lattice distortion leads to considerable variation of dislocation dissociation width, leading to a burst-and-trap character for dislocation motion. Also, the atomistic simulation analysis by Zhang et al.

[102] revealed rugged dislocation lines in the CoCrFeNi HEA with a significant variation in dissociation width of stacking faults. This is radically different with the observations from pure Ni that presents smooth and straight dislocation lines with a uniform width of stacking faults. The distinct dislocation behaviour of HEAs was ascribed to severe lattice distortion due to different atomic sizes and intrinsic properties of individual constituent elements [102,103]. In principle, the local fluctuations in Peierls barriers or SRO leads to a wide spectrum of local critical resolved shear stress and stacking fault energy, allowing synergistic and spatial activation of dislocation slip to delocalize plastic strain [104–106].

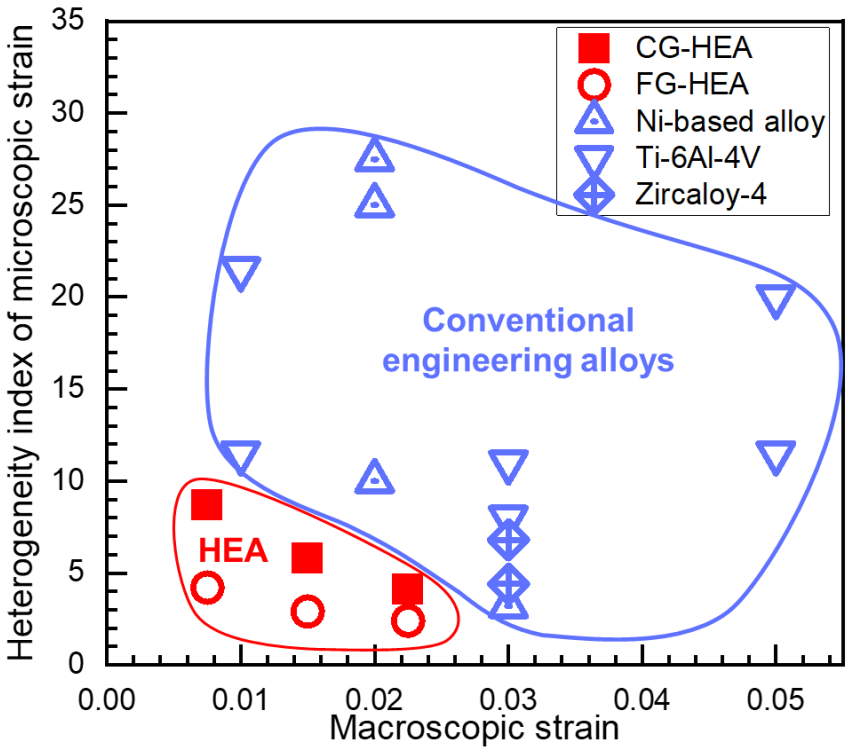

Fig. 10. Heterogeneity index of microscopic strains for the CoCrFeNi HEAs of this work and other engineering alloys with respect to the applied macroscopic strain from Table 6.

4.3. Limitations and outlook

The analysis of this work is limited to the resolution of HRDIC especially for FG-HEA, to 2D comprising solely of x-y in-plane components and missing the z out-of-plane component information, as well as to the surface. For example, during plastic deformation, the stress state of surface and central grains may differ, resulting in discrepancies in the

deformation behaviour between the material's surface and its interior [107,108]. In addition, this work does not consider the possibility of other deformation modes such as stacking faults and deformation twins [16,109–111], and also lacks a quantitative plasticity contribution of grains having slip traces to the macroscopic strain. Moreover, this investigation was limited to one temperature and one FCC HEA with two grain size distributions. The influence of grain size on the microscopic strain localisation behaviour of other HEAs with different microstructures (BCC, HCP, FCC+BCC) at different temperatures should be explored to find out whether the results reported here can be extrapolated to other HEAs [33,55,61,112]. The relationship among the grain size, microscopic strain localisation at the onset of deformation, and final elongation is still unclear, which warrants further research.

In addition, there are another two interesting phenomena, but not the focus of this work, requiring a further investigation. Unlike conventional engineering alloys [33,37,48,60,73,113], the plastic strain is prone to form intragranular slip bands in HEAs (**Appendix Fig. S4**) rather than to strain localisation around grain / twin boundaries. However, the underlying mechanism is still unclear. It should be also noted that the origin of yield plateau is still unclear. More appropriate experimental techniques (such as Video Image Correlation (VIC) that covers a wider area of the specimen) should be considered to assess whether this behaviour can be attributed to the Lüders phenomenon [114].

Therefore, a combined approach of advanced characterization techniques like HRDIC, high resolution - EBSD [115], synchrotron-based X-ray techniques [110,116], crystal plasticity finite element (CPFE) modelling [46,117–121], as well as machine learning approaches [94,122] could elucidate the mechanisms of microscopic strain localisation / heterogeneity of HEAs from different perspectives, and they will be considered in the future. For instance, apart from the DefDAP tool [82], there are several other HRDIC analysis tools, -such as Slip Systems based Local Identification of Plasticity (SSLIP)-, that can identify automatically the active slip systems associated with discrete slip, diffuse slip and cross-slip involving multiple active slip systems [50,69,123]. The incorporation of more advanced characterization techniques and multiple analysis tools could provide a deeper understanding of the influence of grain size on the deformation behaviour of HEA.

5. Conclusions

The statistical distribution of microscopic shear strain in the FCC CoCrFeNi high entropy alloy with different grain sizes was analysed at the onset of plastic deformation using HRDIC. The main conclusions are the following:

1) Microscopic strain localisation increases when the grain size changes from 2.8 ± 1.5 μm to 8.8 ± 5.1 μm in the FCC CoCrFeNi HEA. The higher microscopic strain heterogeneity in CG-HEA is associated with the formation of planar, parallel slip bands within large grains. The presence of transgranular strain bands, that enhance the development of parallel slip bands, further contributes to a high level of microscopic strain localisation in the CG-HEA.

2) The distribution of microscopic strain exhibits a strong dependence on grain size, with distinct slip traces observed within the grains with areas > 20.0 μm^2 and 7.5 μm^2 for CG and FG-HEAs, respectively. This leads to extensive slip traces within the grain interiors of CG-HEA, in comparison to a bi-modal deformation pattern where slip traces are focused within the grains above the critical size in FG-HEA.

3) Multiple slip systems with lower Schmid factor values activate within coarse grains in CG-HEA, while only one or two slip systems, with the 1^{st} and 2^{nd} highest Schmid factors, are active in grains of the FG-HEA. This suggests that the microscopic stress state in CG-HEA is more different than the global stress state as compared to FG-HEA, i.e., higher microscopic deformation heterogeneity in the CG-HEA leads to the activation of less favourable slip systems.

4) Finally, the FCC CoCrFeNi HEAs (particularly the fine-grained one) exhibit a substantially lower level of strain heterogeneity in comparison to a range of engineering alloys at the onset of plastic deformation.

Data availability

The raw HRDIC and EBSD data, the code for HRDIC analysis, as well as microstructural features exported for both the CG-HEA and FG-HEA alloys can be found in Zenodo [doi to be included after this manuscript is accepted].

Declaration of Competing Interest

The authors declare that they have no known competing financial interests or personal relationships that could have appeared to influence the work reported in this paper.

Acknowledgments

Dr. F. Zhang thanks the “National Key Laboratory Foundation of Science and Technology on Materials under Shock and Impact (No. WDZC2022-1)” and “National Natural Science Foundation of China (No. 52271141)”. Additional support is acknowledged from the project "Materiales disruptivos bidimensionales 2D" (MAD2D-CM) funded by Comunidad de Madrid and the Government of Spain by Plan de Recuperación, Transformación y Resiliencia, and the European Union by NextGeneration EU. Mr. B. Yang wishes to express his gratitude for the support of the China Scholarship Council (202106370122). The authors would like to thank Prof. João Quinta da Fonseca for his technical assistance.

Reference

[1] E.P. George, D. Raabe, R.O. Ritchie, High-entropy alloys, Nat. Rev. Mater. 4 (2019) 515–534. https://doi.org/10.1038/s41578-019-0121-4.

[2] L. Han, F. Maccari, I.R. Souza Filho, N.J. Peter, Y. Wei, B. Gault, O. Gutfleisch, Z. Li, D. Raabe, A mechanically strong and ductile soft magnet with extremely low coercivity, Nature 608 (2022) 310–316. https://doi.org/10.1038/s41586-022-04935-3.

[3] B. Gludovatz, A. Hohenwarter, D. Catoor, E.H. Chang, E.P. George, R.O. Ritchie, A fracture-resistant high-entropy alloy for cryogenic applications, Science 345 (2014) 1153–1158. https://doi.org/10.1126/science.1254581.

[4] C. Tandoc, Y.-J. Hu, L. Qi, P.K. Liaw, Mining of lattice distortion, strength, and intrinsic ductility of refractory high entropy alloys, Npj Comput. Mater. 9 (2023) 1–12. https://doi.org/10.1038/s41524-023-00993-x.

[5] B. Cantor, Multicomponent high-entropy Cantor alloys, Prog. Mater. Sci. 120 (2021) 100754. https://doi.org/10.1016/j.pmatsci.2020.100754.

[6] B. Cantor, I.T.H. Chang, P. Knight, A.J.B. Vincent, Microstructural development in equiatomic multicomponent alloys, Mater. Sci. Eng. A 375–377 (2004) 213–218. https://doi.org/10.1016/j.msea.2003.10.257.

[7] X.D. Xu, P. Liu, Z. Tang, A. Hirata, S.X. Song, T.G. Nieh, P.K. Liaw, C.T. Liu, M.W. Chen, Transmission electron microscopy characterization of dislocation structure in a face-centered cubic high-entropy alloy Al0.1CoCrFeNi, Acta Mater. 144 (2018) 107–115. https://doi.org/10.1016/j.actamat.2017.10.050.

[8] L. Patriarca, A. Ojha, H. Sehitoglu, Y.I. Chumlyakov, Slip nucleation in single crystal FeNiCoCrMn high entropy alloy, Scr. Mater. 112 (2016) 54–57. https://doi.org/10.1016/j.scriptamat.2015.09.009.

[9] H.Y. Diao, R. Feng, K.A. Dahmen, P.K. Liaw, Fundamental deformation behavior in high-entropy alloys: An overview, Curr. Opin. Solid State Mater. Sci. 21 (2017) 252–266. https://doi.org/10.1016/j.cossms.2017.08.003.
[10] Y. Wu, W.H. Liu, X.L. Wang, D. Ma, A.D. Stoica, T.G. Nieh, Z.B. He, Z.P. Lu, In-situ neutron diffraction study of deformation behavior of a multi-component high-entropy alloy, Appl. Phys. Lett. 104 (2014) 051910. https://doi.org/10.1063/1.4863748.
[11] Z. Ye, C. Li, M. Zheng, X. Zhang, X. Yang, J. Gu, In situ EBSD/DIC-based investigation of deformation and fracture mechanism in FCC- and L12-structured FeCoNiV high-entropy alloys, Int. J. Plast. 152 (2022) 103247. https://doi.org/10.1016/j.ijplas.2022.103247.
[12] E.P. George, W.A. Curtin, C.C. Tasan, High entropy alloys: A focused review of mechanical properties and deformation mechanisms, Acta Mater. 188 (2020) 435–474. https://doi.org/10.1016/j.actamat.2019.12.015.
[13] Q. Zhang, R. Huang, J. Jiang, T. Cao, Y. Zeng, J. Li, Y. Xue, X. Li, Size effects and plastic deformation mechanisms in single-crystalline CoCrFeNi micro/nanopillars, J. Mech. Phys. Solids 162 (2022) 104853. https://doi.org/10.1016/j.jmps.2022.104853.
[14] Z. Li, S. Zhao, R.O. Ritchie, M.A. Meyers, Mechanical properties of high-entropy alloys with emphasis on face-centered cubic alloys, Prog. Mater. Sci. 102 (2019) 296–345. https://doi.org/10.1016/j.pmatsci.2018.12.003.
[15] G. Laplanche, A. Kostka, O.M. Horst, G. Eggeler, E.P. George, Microstructure evolution and critical stress for twinning in the CrMnFeCoNi high-entropy alloy, Acta Mater. 118 (2016) 152–163. https://doi.org/10.1016/j.actamat.2016.07.038.
[16] B. Wang, H. He, M. Naeem, S. Lan, S. Harjo, T. Kawasaki, Y. Nie, H.W. Kui, T. Ungár, D. Ma, A.D. Stoica, Q. Li, Y. Ke, C.T. Liu, X.-L. Wang, Deformation of CoCrFeNi high entropy alloy at large strain, Scr. Mater. 155 (2018) 54–57. https://doi.org/10.1016/j.scriptamat.2018.06.013.
[17] F. Otto, A. Dlouhý, Ch. Somsen, H. Bei, G. Eggeler, E.P. George, The influences of temperature and microstructure on the tensile properties of a CoCrFeMnNi high-entropy alloy, Acta Mater. 61 (2013) 5743–5755. https://doi.org/10.1016/j.actamat.2013.06.018.
[18] E. Ma, Unusual dislocation behavior in high-entropy alloys, Scr. Mater. 181 (2020) 127–133. https://doi.org/10.1016/j.scriptamat.2020.02.021.
[19] S. Lee, M.J. Duarte, M. Feuerbacher, R. Soler, C. Kirchlechner, C.H. Liebscher, S.H. Oh, G. Dehm, Dislocation plasticity in FeCoCrMnNi high-entropy alloy: quantitative insights from in situ transmission electron microscopy deformation, Mater. Res. Lett. 8 (2020) 216–224. https://doi.org/10.1080/21663831.2020.1741469.
[20] D. Utt, S. Lee, Y. Xing, H. Jeong, A. Stukowski, S.H. Oh, G. Dehm, K. Albe, The origin of jerky dislocation motion in high-entropy alloys, Nat. Commun. 13 (2022) 4777. https://doi.org/10.1038/s41467-022-32134-1.
[21] J. Kumar, A. Linda, K. Biswas, Lattice distortion in FCC HEAs and its effect on mechanical properties: Critical analysis and way forward, J. Appl. Phys. 133 (2023) 155102. https://doi.org/10.1063/5.0144456.
[22] P. Wang, Y. Wu, J. Liu, H. Wang, Impacts of atomic scale lattice distortion on dislocation activity in high-entropy alloys, Extreme Mech. Lett. 17 (2017) 38–42. https://doi.org/10.1016/j.eml.2017.09.015.

[23] S.S. Sohn, A. Kwiatkowski da Silva, Y. Ikeda, F. Körmann, W. Lu, W.S. Choi, B. Gault, D. Ponge, J. Neugebauer, D. Raabe, Ultrastrong Medium-Entropy Single-Phase Alloys Designed via Severe Lattice Distortion, Adv. Mater. 31 (2019) 1807142. https://doi.org/10.1002/adma.201807142.
[24] Y. Guo, T.B. Britton, A.J. Wilkinson, Slip band–grain boundary interactions in commercial-purity titanium, Acta Mater. 76 (2014) 1–12. https://doi.org/10.1016/j.actamat.2014.05.015.
[25] M.T. Andani, A. Lakshmanan, V. Sundararaghavan, J. Allison, A. Misra, Quantitative study of the effect of grain boundary parameters on the slip system level Hall-Petch slope for basal slip system in Mg-4Al, Acta Mater. 200 (2020) 148–161. https://doi.org/10.1016/j.actamat.2020.08.079.
[26] M.-Y. Luo, T.-N. Lam, P.-T. Wang, N.-T. Tsou, Y.-J. Chang, R. Feng, T. Kawasaki, S. Harjo, P.K. Liaw, A.-C. Yeh, S.Y. Lee, J. Jain, E.-W. Huang, Grain-size-dependent microstructure effects on cyclic deformation mechanisms in CoCrFeMnNi high-entropy-alloys, Scr. Mater. 210 (2022) 114459. https://doi.org/10.1016/j.scriptamat.2021.114459.
[27] X. Liu, S. Jiang, J. Lu, J. Wei, D. Wei, F. He, The dual effect of grain size on the strain hardening behaviors of Ni-Co-Cr-Fe high entropy alloys, J. Mater. Sci. Technol. 131 (2022) 177–184. https://doi.org/10.1016/j.jmst.2022.06.001.
[28] S.J. Sun, Y.Z. Tian, H.R. Lin, X.G. Dong, Y.H. Wang, Z.J. Wang, Z.F. Zhang, Temperature dependence of the Hall–Petch relationship in CoCrFeMnNi high-entropy alloy, J. Alloys Compd. 806 (2019) 992–998. https://doi.org/10.1016/j.jallcom.2019.07.357.
[29] S.J. Sun, Y.Z. Tian, H.R. Lin, H.J. Yang, X.G. Dong, Y.H. Wang, Z.F. Zhang, Transition of twinning behavior in CoCrFeMnNi high entropy alloy with grain refinement, Mater. Sci. Eng. A 712 (2018) 603–607. https://doi.org/10.1016/j.msea.2017.12.022.
[30] S. Yoshida, T. Ikeuchi, Y. Bai, N. Tsuji, Effect of Cobalt-Content on Mechanical Properties of Non-Equiatomic Co–Cr–Ni Medium Entropy Alloys, Mater. Trans. 61 (2020) 587–595. https://doi.org/10.2320/matertrans.MT-MK2019004.
[31] J. Li, C. Ding, W. Chen, D. Shan, B. Guo, J. Xu, Strain localization and ductile fracture mechanism of micro/mesoscale deformation in ultrafine-grained pure copper, Mater. Des. 229 (2023) 111873. https://doi.org/10.1016/j.matdes.2023.111873.
[32] R. Zheng, T. Bhattacharjee, S. Gao, W. Gong, A. Shibata, T. Sasaki, K. Hono, N. Tsuji, Change of Deformation Mechanisms Leading to High Strength and Large Ductility in Mg-Zn-Zr-Ca Alloy with Fully Recrystallized Ultrafine Grained Microstructures, Sci. Rep. 9 (2019) 11702. https://doi.org/10.1038/s41598-019-48271-5.
[33] M. Jullien, R.L. Black, J.C. Stinville, M. Legros, D. Texier, Grain size effect on strain localization, slip-grain boundary interaction and damage in the Alloy 718 Ni-based superalloy at 650 °C, Mater. Sci. Eng. A 912 (2024) 146927. https://doi.org/10.1016/j.msea.2024.146927.
[34] D.J. Morrison, V. Chopra, J.W. Jones, Effects of grain size on cyclic strain localization in polycrystalline nickel, Scr. Metall. Mater. 25 (1991) 1299–1304. https://doi.org/10.1016/0956-716X(91)90404-O.

[35] W.Q. Gao, C.L. Zhang, M.X. Yang, S.Q. Zhang, D. Juul Jensen, A. Godfrey, Strain distribution and lattice rotations during in-situ tension of aluminum with a transmodal grain structure, Mater. Sci. Eng. A 828 (2021) 142010. https://doi.org/10.1016/j.msea.2021.142010.
[36] J.C. Stinville, M.A. Charpagne, A. Cervellon, S. Hemery, F. Wang, P.G. Callahan, V. Valle, T.M. Pollock, On the origins of fatigue strength in crystalline metallic materials, Science 377 (2022) 1065–1071. https://doi.org/10.1126/science.abn0392.
[37] D. Lunt, R. Thomas, M. Roy, J. Duff, M. Atkinson, P. Frankel, M. Preuss, J. Quinta da Fonseca, Comparison of sub-grain scale digital image correlation calculated using commercial and open-source software packages, Mater. Charact. 163 (2020) 110271. https://doi.org/10.1016/j.matchar.2020.110271.
[38] Z. Chen, S.H. Daly, Active Slip System Identification in Polycrystalline Metals by Digital Image Correlation (DIC), Exp. Mech. 57 (2017) 115–127. https://doi.org/10.1007/s11340-016-0217-3.
[39] X. Xu, D. Lunt, R. Thomas, R.P. Babu, A. Harte, M. Atkinson, J.Q. da Fonseca, M. Preuss, Identification of active slip mode in a hexagonal material by correlative scanning electron microscopy, Acta Mater. 175 (2019) 376–393. https://doi.org/10.1016/j.actamat.2019.06.024.
[40] D. Yan, C.C. Tasan, D. Raabe, High resolution in situ mapping of microstrain and microstructure evolution reveals damage resistance criteria in dual phase steels, Acta Mater. 96 (2015) 399–409. https://doi.org/10.1016/j.actamat.2015.05.038.
[41] E. Polatidis, W.-N. Hsu, M. Šmíd, H. Van Swygenhoven, A High Resolution Digital Image Correlation Study under Multiaxial Loading, Exp. Mech. 59 (2019) 309–317. https://doi.org/10.1007/s11340-018-00443-6.
[42] C. Bean, F. Wang, M.A. Charpagne, P. Villechaise, V. Valle, S.R. Agnew, D.S. Gianola, T.M. Pollock, J.C. Stinville, Heterogeneous slip localization in an additively manufactured 316L stainless steel, Int. J. Plast. 159 (2022) 103436. https://doi.org/10.1016/j.ijplas.2022.103436.
[43] W. Yin, F. Briffod, H. Hu, T. Shiraiwa, M. Enoki, Three-dimensional configuration of crystal plasticity in stainless steel assessed by high resolution digital image correlation and confocal microscopy, Int. J. Plast. 170 (2023) 103762. https://doi.org/10.1016/j.ijplas.2023.103762.
[44] W. Yin, F. Briffod, H. Hu, K. Yamazaki, T. Shiraiwa, M. Enoki, Role of prior austenite grain boundary and retained austenite in strain localization of medium-carbon high-strength steels, Acta Mater. 281 (2024) 120422. https://doi.org/10.1016/j.actamat.2024.120422.
[45] W. Yin, F. Briffod, H. Hu, K. Yamazaki, T. Shiraiwa, M. Enoki, Quantitative investigation of strain partitioning and failure mechanism in ultrafine grained medium Mn steel through high resolution digital image correlation, Scr. Mater. 229 (2023) 115386. https://doi.org/10.1016/j.scriptamat.2023.115386.
[46] F. Briffod, H. Hu, T. Shiraiwa, M. Enoki, Effect of in-lath slip strength on the strain partitioning in a dual-phase steel investigated by high-resolution digital image correlation and crystal plasticity simulations, Mater. Sci. Eng. A 862 (2023) 144413. https://doi.org/10.1016/j.msea.2022.144413.
[47] B. Yavuzyegit, E. Avcu, A.D. Smith, J.M. Donoghue, D. Lunt, J.D. Robson, T.L. Burnett, J.Q. da Fonseca, P.J. Withers, Mapping plastic deformation mechanisms in

AZ31 magnesium alloy at the nanoscale, Acta Mater. 250 (2023) 118876. https://doi.org/10.1016/j.actamat.2023.118876.
[48] A. Orozco-Caballero, D. Lunt, J.D. Robson, J. Quinta da Fonseca, How magnesium accommodates local deformation incompatibility: A high-resolution digital image correlation study, Acta Mater. 133 (2017) 367–379. https://doi.org/10.1016/j.actamat.2017.05.040.
[49] F. Briffod, Y. Shen, H. Hu, W. Yin, T. Shiraiwa, M. Enoki, Effect of microstructure on the deformation of as-cast α-Mg/LPSO two-phase alloys: An integrated SEM-DIC and crystal plasticity study, Materialia 33 (2024) 102015. https://doi.org/10.1016/j.mtla.2024.102015.
[50] R. Ni, C.J. Boehlert, Y. Zeng, B. Chen, S. Huang, J. Zheng, H. Zhou, Q. Wang, D. Yin, Automated analysis framework of strain partitioning and deformation mechanisms via multimodal fusion and computer vision, Int. J. Plast. 182 (2024) 104119. https://doi.org/10.1016/j.ijplas.2024.104119.
[51] G. Garcés, A. Orozco-Caballero, J. Quinta da Fonseca, P. Pérez, J. Medina, A. Stark, N. Schell, P. Adeva, Initial plasticity stages in Mg alloys containing Long-Period Stacking Ordered phases using High Resolution Digital Image Correlation (HRDIC) and in-situ synchrotron radiation, Mater. Sci. Eng. A 772 (2020) 138716. https://doi.org/10.1016/j.msea.2019.138716.
[52] A. Orozco-Caballero, T. Jackson, J.Q. da Fonseca, High-resolution digital image correlation study of the strain localization during loading of a shot-peened RR1000 nickel-based superalloy, Acta Mater. 220 (2021) 117306. https://doi.org/10.1016/j.actamat.2021.117306.
[53] A. Harte, M. Atkinson, A. Smith, C. Drouven, S. Zaefferer, J. Quinta da Fonseca, M. Preuss, The effect of solid solution and gamma prime on the deformation modes in Ni-based superalloys, Acta Mater. 194 (2020) 257–275. https://doi.org/10.1016/j.actamat.2020.04.004.
[54] A. Harte, M. Atkinson, M. Preuss, J. Quinta da Fonseca, A statistical study of the relationship between plastic strain and lattice misorientation on the surface of a deformed Ni-based superalloy, Acta Mater. 195 (2020) 555–570. https://doi.org/10.1016/j.actamat.2020.05.029.
[55] D. Texier, J. Milanese, M. Jullien, J. Genée, J.-C. Passieux, D. Bardel, E. Andrieu, M. Legros, J.-C. Stinville, Strain localization in the Alloy 718 Ni-based superalloy: From room temperature to 650 °C, Acta Mater. 268 (2024) 119759. https://doi.org/10.1016/j.actamat.2024.119759.
[56] Z. Zhang, Z. Yang, S. Lu, A. Harte, R. Morana, M. Preuss, Strain localisation and failure at twin-boundary complexions in nickel-based superalloys, Nat. Commun. 11 (2020) 4890. https://doi.org/10.1038/s41467-020-18641-z.
[57] J.M. Hestroffer, J.-C. Stinville, M.-A. Charpagne, M.P. Miller, T.M. Pollock, I.J. Beyerlein, Slip localization behavior at triple junctions in nickel-base superalloys, Acta Mater. 249 (2023) 118801. https://doi.org/10.1016/j.actamat.2023.118801.
[58] M.D. Atkinson, J.M. Donoghue, J.Q. da Fonseca, Measurement of local plastic strain during uniaxial reversed loading of nickel alloy 625, Mater. Charact. 168 (2020) 110561. https://doi.org/10.1016/j.matchar.2020.110561.
[59] J.H. Liu, N. Vanderesse, J.-C. Stinville, T.M. Pollock, P. Bocher, D. Texier, In-plane and out-of-plane deformation at the sub-grain scale in polycrystalline materials

assessed by confocal microscopy, Acta Mater. 169 (2019) 260–274. https://doi.org/10.1016/j.actamat.2019.03.001.
[60] J.C. Stinville, N. Vanderesse, F. Bridier, P. Bocher, T.M. Pollock, High resolution mapping of strain localization near twin boundaries in a nickel-based superalloy, Acta Mater. 98 (2015) 29–42. https://doi.org/10.1016/j.actamat.2015.07.016.
[61] D. Anjaria, M. Heczko, R.L. Black, C. Bean, M.A. Reynolds, K. Zhang, D. Texier, V. Valle, M.J. Mills, D.C. Pagan, J.C. Stinville, Plastic deformation delocalization at cryogenic temperatures in a nickel-based superalloy, Acta Mater. 276 (2024) 120106. https://doi.org/10.1016/j.actamat.2024.120106.
[62] D. Lunt, X. Xu, T. Busolo, J. Quinta da Fonseca, M. Preuss, Quantification of strain localisation in a bimodal two-phase titanium alloy, Scr. Mater. 145 (2018) 45–49. https://doi.org/10.1016/j.scriptamat.2017.10.012.
[63] D. Lunt, R. Thomas, M.D. Atkinson, A. Smith, R. Sandala, J.Q. da Fonseca, M. Preuss, Understanding the role of local texture variation on slip activity in a two-phase titanium alloy, Acta Mater. 216 (2021) 117111. https://doi.org/10.1016/j.actamat.2021.117111.
[64] E. Nieto-Valeiras, A. Orozco-Caballero, M. Sarebanzadeh, J. Sun, J. LLorca, Analysis of slip transfer across grain boundaries in Ti via diffraction contrast tomography and high-resolution digital image correlation: When the geometrical criteria are not sufficient, Int. J. Plast. 175 (2024) 103941. https://doi.org/10.1016/j.ijplas.2024.103941.
[65] J.C. Stinville, W. Ludwig, P.G. Callahan, M.P. Echlin, V. Valle, T.M. Pollock, H. Proudhon, Observation of bulk plasticity in a polycrystalline titanium alloy by diffraction contrast tomography and topotomography, Mater. Charact. 188 (2022) 111891. https://doi.org/10.1016/j.matchar.2022.111891.
[66] S. Hémery, J.C. Stinville, F. Wang, M.A. Charpagne, M.G. Emigh, T.M. Pollock, V. Valle, Strain localization and fatigue crack formation at (0001) twist boundaries in titanium alloys, Acta Mater. 219 (2021) 117227. https://doi.org/10.1016/j.actamat.2021.117227.
[67] D. Lunt, T. Busolo, X. Xu, J. Quinta da Fonseca, M. Preuss, Effect of nanoscale α 2 precipitation on strain localisation in a two-phase Ti-alloy, Acta Mater. 129 (2017) 72–82. https://doi.org/10.1016/j.actamat.2017.02.068.
[68] D. Lunt, J.Q. da Fonseca, D. Rugg, M. Preuss, Slip Band Characterisation in Ti-6Al-4V with Varying Degrees of Macrozones, in: Proc. 13th World Conf. Titan., John Wiley & Sons, Ltd, 2016: pp. 1129–1134. https://doi.org/10.1002/9781119296126.ch191.
[69] H. Hu, F. Briffod, T. Shiraiwa, M. Enoki, Automated slip system identification and strain analysis framework using high-resolution digital image correlation data: Application to a bimodal Ti-6Al-4V alloy, Int. J. Plast. 166 (2023) 103618. https://doi.org/10.1016/j.ijplas.2023.103618.
[70] H. Hu, F. Briffod, W. Yin, T. Shiraiwa, M. Enoki, Quantitative investigation of slip band activities in a bimodal titanium alloy under pure fatigue and dwell-fatigue loadings, Int. J. Fatigue 182 (2024) 108203. https://doi.org/10.1016/j.ijfatigue.2024.108203.
[71] C. Bean, J.C. Stinville, A. Naït-Ali, Z. Wu, F. Sun, F. Prima, S. Hémery, Microstructural statistics for low-cycle fatigue crack initiation in α+β titanium alloys: A

microstructure based RVE assessment, Int. J. Fatigue 176 (2023) 107854. https://doi.org/10.1016/j.ijfatigue.2023.107854.
[72] T. Giroud, P. Villechaise, A. Naït-Ali, D. Mellier, S. Hémery, Anisotropy in tensile properties of a high strength metastable β titanium alloy, Mater. Des. 247 (2024) 113401. https://doi.org/10.1016/j.matdes.2024.113401.
[73] R. Thomas, D. Lunt, M.D. Atkinson, J. Quinta da Fonseca, M. Preuss, F. Barton, J. O'Hanlon, P. Frankel, Characterisation of irradiation enhanced strain localisation in a zirconium alloy, Materialia 5 (2019) 100248. https://doi.org/10.1016/j.mtla.2019.100248.
[74] R. Thomas, D. Lunt, M.D. Atkinson, J.Q. da Fonseca, M. Preuss, P. Honniball, P. Frankel, The role of hydrides and precipitates on the strain localisation behaviour in a zirconium alloy, Acta Mater. 261 (2023) 119327. https://doi.org/10.1016/j.actamat.2023.119327.
[75] J.P. Goulmy, D. Depriester, F. Guittonneau, L. Barrallier, S. Jégou, Mechanical behavior of polycrystals: Coupled in situ DIC-EBSD analysis of pure copper under tensile test, Mater. Charact. 194 (2022) 112322. https://doi.org/10.1016/j.matchar.2022.112322.
[76] Y.F. Wang, C.X. Huang, Q. He, F.J. Guo, M.S. Wang, L.Y. Song, Y.T. Zhu, Heterostructure induced dispersive shear bands in heterostructured Cu, Scr. Mater. 170 (2019) 76–80. https://doi.org/10.1016/j.scriptamat.2019.05.036.
[77] Y. Chong, T. Bhattacharjee, Y. Tian, A. Shibata, N. Tsuji, Deformation mechanism of bimodal microstructure in Ti-6Al-4V alloy: The effects of intercritical annealing temperature and constituent hardness, J. Mater. Sci. Technol. 71 (2021) 138–151. https://doi.org/10.1016/j.jmst.2020.08.057.
[78] Y. Yang, Y. Gong, X. Li, H. Liu, C. Li, J. Yang, H. Pan, B. Shu, C. Deng, J. Fang, X. Zhu, Effect of bimodal grain size and gradient structure on heterogeneous deformation induced (HDI) stress and mechanical properties of Cu, Mater. Res. Express 9 (2022) 035004. https://doi.org/10.1088/2053-1591/ac5a37.
[79] F. Di Gioacchino, J. Quinta da Fonseca, Plastic Strain Mapping with Sub-micron Resolution Using Digital Image Correlation, Exp. Mech. 53 (2013) 743–754. https://doi.org/10.1007/s11340-012-9685-2.
[80] S. Preibisch, S. Saalfeld, P. Tomancak, Globally optimal stitching of tiled 3D microscopic image acquisitions, Bioinformatics 25 (2009) 1463–1465. https://doi.org/10.1093/bioinformatics/btp184.
[81] J. Schindelin, I. Arganda-Carreras, E. Frise, V. Kaynig, M. Longair, T. Pietzsch, S. Preibisch, C. Rueden, S. Saalfeld, B. Schmid, J.-Y. Tinevez, D.J. White, V. Hartenstein, K. Eliceiri, P. Tomancak, A. Cardona, Fiji: an open-source platform for biological-image analysis, Nat. Methods 9 (2012) 676–682. https://doi.org/10.1038/nmeth.2019.
[82] M.D. Atkinson, R. Thomas, A. Harte, P. Crowther, J. Quinta da Fonseca, DefDAP: Deformation Data Analysis in Python, Zenodo, 2020. https://doi.org/10.5281/zenodo.3688097.
[83] J.D. Hunter, Matplotlib: A 2D Graphics Environment, Comput. Sci. Eng. 9 (2007) 90–95. https://doi.org/10.1109/MCSE.2007.55.
[84] R. Thomas, D. Lunt, M.D. Atkinson, J. Quinta da Fonseca, M. Preuss, F. Barton, J. O'Hanlon, P. Frankel, The Effect of Loading Direction on Slip and Twinning in an

Irradiated Zirconium Alloy, in: Zircon. Nucl. Ind. 19th Int. Symp., ASTM International, 100 Barr Harbor Drive, PO Box C700, West Conshohocken, PA 19428-2959, 2021: pp. 233–261. https://doi.org/10.1520/STP162220190027.

[85] P. van Liempt, C. Bos, J. Sietsma, A physically based yield criterion II. Incorporation of Hall Petch effect and resistance due to thermally activated dislocation glide, Mater. Sci. Eng. A 652 (2016) 7–13. https://doi.org/10.1016/j.msea.2015.11.035.

[86] M.N. Shiekhelsouk, V. Favier, K. Inal, M. Cherkaoui, Modelling the behaviour of polycrystalline austenitic steel with twinning-induced plasticity effect, Int. J. Plast. 25 (2009) 105–133. https://doi.org/10.1016/j.ijplas.2007.11.004.

[87] J. Reiser, A. Hartmaier, Elucidating the dual role of grain boundaries as dislocation sources and obstacles and its impact on toughness and brittle-to-ductile transition, Sci. Rep. 10 (2020) 2739. https://doi.org/10.1038/s41598-020-59405-5.

[88] F. Jiang, C. Zhao, D. Liang, W. Zhu, Y. Zhang, S. Pan, F. Ren, In-situ formed heterogeneous grain structure in spark-plasma-sintered CoCrFeMnNi high-entropy alloy overcomes the strength-ductility trade-off, Mater. Sci. Eng. A 771 (2020) 138625. https://doi.org/10.1016/j.msea.2019.138625.

[89] A. Oudriss, J. Creus, J. Bouhattate, E. Conforto, C. Berziou, C. Savall, X. Feaugas, Grain size and grain-boundary effects on diffusion and trapping of hydrogen in pure nickel, Acta Mater. 60 (2012) 6814–6828. https://doi.org/10.1016/j.actamat.2012.09.004.

[90] L. Wang, K. Du, C. Yang, J. Teng, L. Fu, Y. Guo, Z. Zhang, X. Han, In situ atomic-scale observation of grain size and twin thickness effect limit in twin-structural nanocrystalline platinum, Nat. Commun. 11 (2020) 1167. https://doi.org/10.1038/s41467-020-14876-y.

[91] X. Li, H. Long, J. Zhang, D. Ma, D. Kong, Y. Lu, S. Sun, J. Cai, X. Wang, L. Wang, S. Mao, Direct observation of the grain boundaries acting as dislocation sources in nanocrystalline platinum, Mater. Charact. 181 (2021) 111493. https://doi.org/10.1016/j.matchar.2021.111493.

[92] Y. Gao, Y. Ding, H. Li, H. Dong, R. Zhang, J. Li, Q. Luo, Grain-size dependent elastic-plastic deformation behaviour of inconel 625 alloy studied by in-situ neutron diffraction, Intermetallics 138 (2021) 107340. https://doi.org/10.1016/j.intermet.2021.107340.

[93] B. Yang, L. Javier, Origin of nucleation and growth of extension twins in grains unsuitably oriented for twinning during deformation of Mg-1%Al, J. Magnes. Alloys (2024) In press. https://doi.org/10.1016/j.jma.2024.02.013.

[94] B. Yang, V. Vassilev-Galindo, J. LLorca, Application of machine learning to assess the influence of microstructure on twin nucleation in Mg alloys, Npj Comput. Mater. 10 (2023) 26. https://doi.org/10.1038/s41524-024-01212-x.

[95] D. Lunt, A. Ho, A. Davis, A. Harte, F. Martina, J. Quinta da Fonseca, P. Prangnell, The effect of loading direction on strain localisation in wire arc additively manufactured Ti–6Al–4V, Mater. Sci. Eng. A 788 (2020) 139608. https://doi.org/10.1016/j.msea.2020.139608.

[96] E. Ma, X. Wu, Tailoring heterogeneities in high-entropy alloys to promote strength–ductility synergy, Nat. Commun. 10 (2019) 5623. https://doi.org/10.1038/s41467-019-13311-1.

[97] Y.F. Ye, Q. Wang, J. Lu, C.T. Liu, Y. Yang, High-entropy alloy: challenges and prospects, Mater. Today 19 (2016) 349–362. https://doi.org/10.1016/j.mattod.2015.11.026.
[98] S. Moore, R. Burrows, D. Kumar, M.B. Kloucek, A.D. Warren, P.E.J. Flewitt, L. Picco, O.D. Payton, T.L. Martin, Observation of stress corrosion cracking using real-time in situ high-speed atomic force microscopy and correlative techniques, Npj Mater. Degrad. 5 (2021) 1–10. https://doi.org/10.1038/s41529-020-00149-y.
[99] M.R. Barnett, Twinning and the ductility of magnesium alloys: Part II. “Contraction” twins, Mater. Sci. Eng. A 464 (2007) 8–16. https://doi.org/10.1016/j.msea.2007.02.109.
[100] A. Needleman, J.R. Rice, Limits to Ductility Set by Plastic Flow Localization, in: D.P. Koistinen, N.-M. Wang (Eds.), Mech. Sheet Met. Form. Mater. Behav. Deform. Anal., Springer US, Boston, MA, 1978: pp. 237–267. https://doi.org/10.1007/978-1-4613-2880-3_10.
[101] M. Cervera, J.-Y. Wu, S. Kim, M. Chiumenti, On the mechanics of strain localization in plasticity: isotropic and orthotropic, elasto- and rigid-plastic, associated and non-associated models, Acta Mech. 233 (2022) 1513–1542. https://doi.org/10.1007/s00707-022-03184-9.
[102] Q. Zhang, R. Niu, Y. Liu, J. Jiang, F. Xu, X. Zhang, J.M. Cairney, X. An, X. Liao, H. Gao, X. Li, Room-temperature super-elongation in high-entropy alloy nanopillars, Nat. Commun. 14 (2023) 7469. https://doi.org/10.1038/s41467-023-42894-z.
[103] Q. Ding, Y. Zhang, X. Chen, X. Fu, D. Chen, S. Chen, L. Gu, F. Wei, H. Bei, Y. Gao, M. Wen, J. Li, Z. Zhang, T. Zhu, R.O. Ritchie, Q. Yu, Tuning element distribution, structure and properties by composition in high-entropy alloys, Nature 574 (2019) 223–227. https://doi.org/10.1038/s41586-019-1617-1.
[104] W. Li, S. Lyu, Y. Chen, A.H.W. Ngan, Fluctuations in local shear-fault energy produce unique and dominating strengthening in metastable complex concentrated alloys, Proc. Natl. Acad. Sci. U. S. A. 120 (n.d.) e2209188120. https://doi.org/10.1073/pnas.2209188120.
[105] Y. Osetsky, J. Morris, On the origin of internal obstacles to dislocation glide in single-phase NiFe random alloys, Acta Mater. 222 (2022) 117457. https://doi.org/10.1016/j.actamat.2021.117457.
[106] L. Zhu, Z. Wu, Effects of short range ordering on the generalized stacking fault energy and deformation mechanisms in FCC multiprincipal element alloys, Acta Mater. 259 (2023) 119230. https://doi.org/10.1016/j.actamat.2023.119230.
[107] C. Bing, T.R. Bieler, P. Eisenlohr, A computational study of how surfaces affect slip family activity, Acta Mater. 259 (2023) 119246. https://doi.org/10.1016/j.actamat.2023.119246.
[108] A. Chakraborty, C. Zhang, S. Balachandran, T.R. Bieler, P. Eisenlohr, Assessment of surface and bulk-dominated methodologies to measure critical resolved shear stresses in hexagonal materials, Acta Mater. 184 (2020) 241–253. https://doi.org/10.1016/j.actamat.2019.11.023.
[109] Y. Wu, S. Liu, K. Luo, C. Kong, H. Yu, Deformation mechanism and mechanical properties of a CoCrFeNi high-entropy alloy via room-temperature rolling, cryorolling, and asymmetric cryorolling, J. Alloys Compd. 960 (2023) 170883. https://doi.org/10.1016/j.jallcom.2023.170883.

[110] T. Cao, Q. Zhang, L. Wang, L. Wang, Y. Xiao, J. Yao, H. Liu, Y. Ren, J. Liang, Y. Xue, X. Li, Dynamic deformation behaviors and mechanisms of CoCrFeNi high-entropy alloys, Acta Mater. 260 (2023) 119343. https://doi.org/10.1016/j.actamat.2023.119343.
[111] W. Huo, H. Zhou, F. Fang, X. Hu, Z. Xie, J. Jiang, Strain-rate effect upon the tensile behavior of CoCrFeNi high-entropy alloys, Mater. Sci. Eng. A 689 (2017) 366–369. https://doi.org/10.1016/j.msea.2017.02.077.
[112] S.Y. Peng, Y.Z. Tian, Z.Y. Ni, S. Lu, S. Li, Effect of grain size on the deformation mechanism and fracture behavior of a non-equiatomic CoCrNi alloy with low stacking fault energy, Int. J. Plast. 182 (2024) 104129. https://doi.org/10.1016/j.ijplas.2024.104129.
[113] Y. Xuan, J. Chang, Y. Ou, R. Yang, Z. Zhang, Heterogeneous structure architected by additive manufacturing: facile route towards strong and ductile steel, Mater. Res. Lett. 12 (2024) 199–207. https://doi.org/10.1080/21663831.2024.2314145.
[114] H. Rezayat, H. Ghassemi-Armaki, S.P. Bhat, S. Sriram, S.S. Babu, Constitutive properties and plastic instabilities in the heat-affected zones of advanced high-strength steel spot welds, J. Mater. Sci. 54 (2019) 5825–5843. https://doi.org/10.1007/s10853-018-03276-9.
[115] T.E.J. Edwards, X. Maeder, J. Ast, L. Berger, J. Michler, Mapping pure plastic strains against locally applied stress: Revealing toughening plasticity, Sci. Adv. 8 (2022) eabo5735. https://doi.org/10.1126/sciadv.abo5735.
[116] H.S. Oh, M. Xu, S. Wei, F.F. Worsnop, J.M. LeBeau, C.C. Tasan, Composition-dependent transformation-induced plasticity in Co-based complex concentrated alloys, Acta Mater. 262 (2024) 119349. https://doi.org/10.1016/j.actamat.2023.119349.
[117] D. Hu, Z. Guo, N. Grilli, A. Tay, Z. Lu, W. Yan, Understanding the strain localization in additively manufactured materials: Micro-scale tensile tests and crystal plasticity modeling, Int. J. Plast. 177 (2024) 103981. https://doi.org/10.1016/j.ijplas.2024.103981.
[118] D. Agius, A. Kareer, A.A. Mamun, C. Truman, D.M. Collins, M. Mostafavi, D. Knowles, A crystal plasticity model that accounts for grain size effects and slip system interactions on the deformation of austenitic stainless steels, Int. J. Plast. 152 (2022) 103249. https://doi.org/10.1016/j.ijplas.2022.103249.
[119] C. Liu, F. Roters, D. Raabe, Finite strain crystal plasticity-phase field modeling of twin, dislocation, and grain boundary interaction in hexagonal materials, Acta Mater. 242 (2023) 118444. https://doi.org/10.1016/j.actamat.2022.118444.
[120] S. Haouala, J. Segurado, J. LLorca, An analysis of the influence of grain size on the strength of FCC polycrystals by means of computational homogenization, Acta Mater. 148 (2018) 72–85. https://doi.org/10.1016/j.actamat.2018.01.024.
[121] D. Depriester, J. Goulmy, L. Barrallier, Slip identification from HR-DIC/EBSD: Incorporating Crystal Plasticity constitutive laws, Int. J. Solids Struct. 305 (2024) 113077. https://doi.org/10.1016/j.ijsolstr.2024.113077.
[122] D. Kuriki, F. Briffod, T. Shiraiwa, M. Enoki, Multimodal deep learning framework to predict strain localization of Mg/LPSO two-phase alloys, Acta Mater. 281 (2024) 120398. https://doi.org/10.1016/j.actamat.2024.120398.

[123] T. Vermeij, R.H.J. Peerlings, M.G.D. Geers, J.P.M. Hoefnagels, Automated identification of slip system activity fields from digital image correlation data, Acta Mater. 243 (2023) 118502. https://doi.org/10.1016/j.actamat.2022.118502.